

# Growing and Trapping Pebbles with Fragile Collisions of Particles in Protoplanetary Disks

Paola Pinilla and Christian T. Lenz

Max-Planck-Institut für Astronomie, Königstuhl 17, 69117, Heidelberg, Germany, e-mail: [pinilla@mpia.de](mailto:pinilla@mpia.de), e-mail: [lenz@mpia.de](mailto:lenz@mpia.de)

## ABSTRACT

Recent laboratory experiments indicate that destructive collisions of icy dust particles occur with much lower velocities than previously thought. These fragmentation velocities play a crucial role in planet formation because they set the maximum grain size in collisional growth models. When considering these new velocities from laboratory experiments in dust evolution models, growing to pebble sizes (typically millimeter to decimeter sized particles) in protoplanetary disks is difficult, which may contradict (sub-) millimeter observations and challenge the formation of planetesimals and planets. We investigate what conditions are required in dust evolution models to grow and trap pebbles in protoplanetary disks when the fragmentation speed is  $1 \text{ m s}^{-1}$  in the entire disk. In particular, we disentangle the parameters controlling the effects of turbulent velocities ( $\delta_t$ ), vertical stirring ( $\delta_z$ ), radial diffusion ( $\delta_r$ ), and gas viscous evolution ( $\alpha$ ), always assuming that particles cannot diffuse faster (radially or vertically) than the gas (i.e.,  $\delta_{r,z,t} \leq \alpha$ ). We compare our models with observations of protoplanetary disks at both the near-infrared and millimeter regimes. To form pebbles and have effective particle trapping, the parameter that controls the particle turbulent velocities must be low ( $\delta_t \lesssim 10^{-4}$ ). In these cases, the vertical settling can limit the formation of pebbles, which also prevents particle trapping. Therefore, the parameter that sets the vertical settling and stirring of the grains must be  $\delta_z < 10^{-3}$ . Our results suggest that different combinations of the particle and gas diffusion parameters can lead to a large diversity of millimeter fluxes and dust disk radii. When pebble formation happens and trapping is efficient, gaps and rings have higher contrast at millimeter emission than at near-infrared. In the case of inefficient trapping, structures are also formed at the two wavelengths, producing deeper and wider gaps in the near-infrared. Our results highlight the importance to obtain observational constraints of gas and particle diffusion parameters and the properties of gaps at short and long wavelengths to better understand basic features of protoplanetary disks and the origin of the seen structures in these objects.

**Key words.** accretion, accretion disk – circumstellar matter – stars: pre-main-sequence – protoplanetary disk – planet formation

## 1. Introduction

Planet formation happens in protoplanetary disks, which are mainly composed by gas, but most of the information that we have about planets forming in disks comes from the dust that dominates the disk opacity. The initial properties of the dust in disks are inherited from the interstellar medium, such as its size and composition. These initial properties are expected to change by different physical processes that lead to collisions and transport of the particles (see e.g., [Birnstiel et al. 2016](#), for a review).

The growth of particles from (sub-)micron-sized dust to pebbles is fundamental to understand the first steps of planet formation. From the observational point of view, we can have access to this process by observing the distribution of micron-sized dust to pebbles (sub-mm to centimeter sized particles) with observations from the optical to centimeter wavelengths, respectively. Solid bodies larger than centimeter-sized particles have very low opacities and we are blind from the observational point of view about what happens from the formation of pebbles to planets. To connect current theories of planet formation with observations, we rely on connecting our observational knowledge of the small bodies (up to pebbles) to exoplanets statistics.

Recent deep high angular resolution observations of protoplanetary disks have evidenced the existence of structures in these objects, such as rings, gaps, spiral arms and lopsided shapes (e.g., [Andrews 2020](#)). These structures are believed to be regions of high pressure where the radial drift of pebbles is reduced or stopped completely ([Whipple 1972](#)), and where planetesimal formation can happen (e.g., [Pinilla et al. 2012, 2020](#); [Dullemond et al. 2018](#); [Lenz et al. 2019](#); [Stammler et al. 2019](#); [Klahr & Schreiber 2020](#)). The current understanding of these structures, from the observational and theoretical point of view is driving the field of planet-forming disks.

Another crucial part to understand the first growth from interstellar medium dust to pebbles is laboratory experiments of particle collisions. They provide the potential outputs after collisions with a given initial relative velocity. Potential outputs include sticking, fragmentation, bouncing, or mass transfer (e.g., [Windmark et al. 2012](#)). They also impart the limits for theoreticians about thresholds of velocities to have effective growth or destructive collisions (e.g., [Blum & Wurm 2000, 2008](#); [Kimura et al. 2015, 2020](#)). These experiments are, however, challenging because their conditions aim at being as close as possible to the phys-

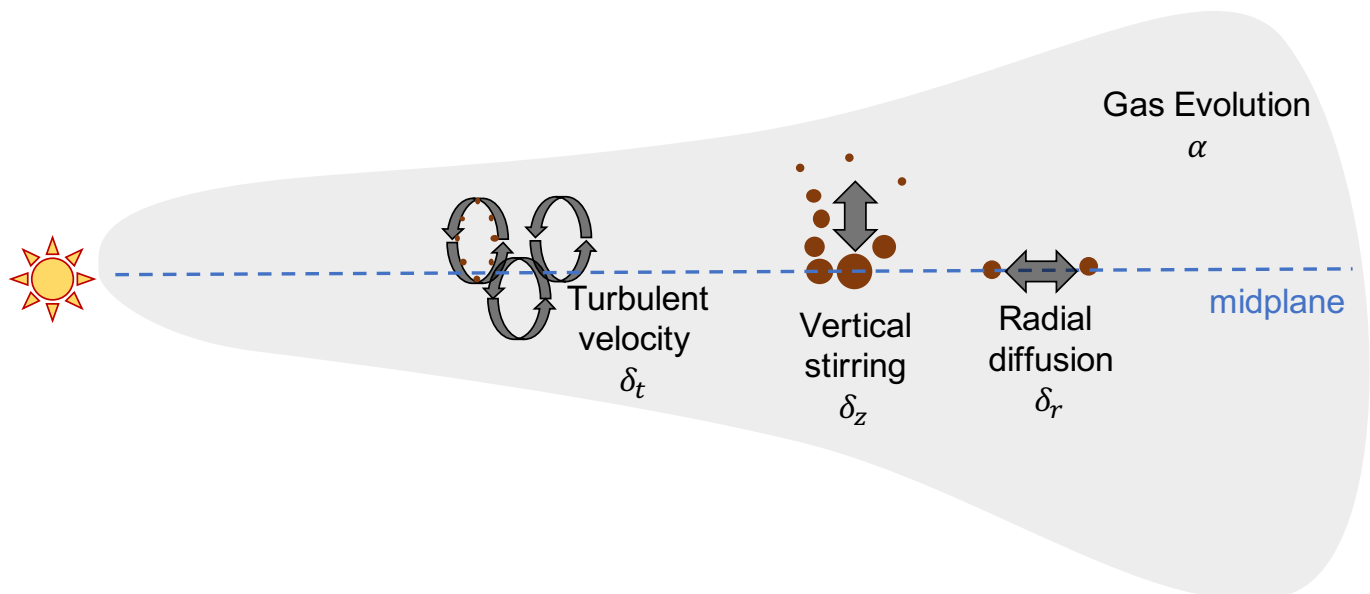


**Fig. 1.** Schematic view of turbulent velocities, vertical stirring/settling, and radial diffusion of dust. In the standard models, all of them are set to a value that depends on the  $\alpha$  parameter that regulates the gas viscous evolution. In this paper, all four parameters are assumed to be independent.

cal properties of disks, such as low densities, pressure, and temperatures.

It was commonly thought that water ice particles are more sticky than silicates (Blum & Wurm 2000; Wada et al. 2009, 2011; Gundlach & Blum 2015; Musiolik et al. 2016), as snow balls vs. sand; with at least one order of magnitude of difference in the fragmentation velocity between these two species. Having high fragmentation velocities for icy particles strongly helps to form pebbles in the disk, since the maximum grain size in the fragmentation dominated regime is proportional to the square of the threshold of the fragmentation velocity (e.g. Brauer et al. 2008; Birnstiel et al. 2010). Nonetheless, recent laboratory experiments have been able to get closer to the temperatures of protoplanetary disks, changing our perspective of collisional growth by concluding that amorphous water ice particles are as or even more fragile than silicates (Gundlach et al. 2018; Musiolik & Wurm 2019; Steinpilz et al. 2019). These experiments aim to measure the sticking force when two particles are in contact, which depends on the surface energy of the grains and therefore on the particle composition (e.g., Kimura et al. 2015). Most of the classical experiments used mono-layer dust particles, with insignificant amount of water or no water at all. This limitation comes from keeping low values of temperature and pressure, and most of the information that we previously had about collision of (water) ices came from numerical experiments. More recent laboratory experiments manage to keep low values of temperature in their collisions ( $<180$  K) and show that the surface energy of these grains decrease, in contradiction with previous assumptions of collisions of water ice particles.

The results of these new experiments suggest that the fragmentation velocities for icy particles is  $1 \text{ m s}^{-1}$  or even lower. This not only brings a problem for the formation of pebbles, and hence for the formation of planets as a whole, but also it makes the current interpretation of disk observations challenging. If the current structures are the by-product of pressure bumps trapping the particles, grains have to grow at least to sub-millimeter sizes to efficiently

slow down their drift at the pressure bump and be trapped. If particles remain small (typically  $\lesssim 0.1 \text{ mm}$ ), radial drift is slow and other effects such as turbulent mixing and radial diffusion may become more important, preventing the grains to be trapped. Although the maximum grain size that particles may reach with fragmentation velocities of  $1 \text{ m s}^{-1}$  may be in agreement with the maximum grain size proposed by Liu (2019) and Zhu et al. (2019), to explain the optical depth of several disks recently observed with the Atacama Large Millimeter/submillimeter Array (ALMA) when considering self-scattering.

In this paper, we investigate what conditions are required in dust evolution models to grow and trap pebbles in protoplanetary disks when the fragmentation speed is  $1 \text{ m s}^{-1}$ . The main question that we aim to answer is: if the fragmentation velocities are as suggested from laboratory experiments, what values of turbulence, settling and diffusion are needed to grow to pebbles and have particle trapping? when comparing with observed properties of protoplanetary disks, what would be a reasonable value for the parameter that controls the gas viscous evolution vs. the dust evolution? To answer these questions, we investigate parameters that rule the turbulent velocities ( $\delta_t$ ), vertical stirring ( $\delta_z$ ), radial diffusion ( $\delta_r$ ), and viscous gas evolution ( $\alpha$ ), and consider that they are independent from each other. We aim to disentangle the effect of each of these physical processes by always assuming that particles should not diffuse faster than the gas (i.e.,  $\delta_{r,z,t} \leq \alpha$ ). To test our models, we combine the results with radiative transfer simulations, in order to compare with observations at near-infrared and millimeter emission.

This paper is organized as follows. In the next section, we give a brief overview of the models and the parameters that are assumed for the angular momentum transport of gas and dust (vertical and radial) diffusion. In this section, we also describe our assumptions for the radiative transfer calculations. In Sect. 3, we present the results of our models. In Sect. 4, we discuss our results in the context of different observational diagnostics, such as millimeter fluxes, dust

disk radii, images, and spectral indices. Section 5 summarizes the conclusions of this work.

## 2. Models

### 2.1. Dust Evolution Models

We used the `dustpy` code developed by Stammer & Birnstiel (in prep) based on the dust evolution models from Birnstiel et al. (2010). This code solves the Smoluchowski coagulation equation (Smoluchowski 1916) simultaneously with the transport of the grains. Dust particles collide with each other and are transported in the disk by different mechanisms: thermal Brownian motion, vertical stirring/settling, turbulent mixing, and azimuthal/radial drift. All of these velocities are taken into account to calculate the relative velocities before collision. The output after collision (coagulation, fragmentation, or erosion) is obtained by comparing the relative velocities with the fragmentation speed  $v_f$ , a parameter that we set to  $1 \text{ m s}^{-1}$  in the entire disk based on recent laboratory experiments.

Most of the transport and dynamics of the particles are regulated by the interaction of the dust particles with the gas. The dimensionless Stokes number quantifies the importance of the drag forces on the dynamics of the particles by comparing the stopping time of the particles to the Keplerian frequency at a given disk location. In the Epstein drag regime (Epstein 1924) and near to the disk midplane, the Stokes number is defined as (Brauer et al. 2008; Birnstiel et al. 2010)

$$\text{St} = \frac{a \rho_s \pi}{\Sigma_g} \frac{\pi}{2}, \quad (1)$$

where  $a$  is the grain size,  $\rho_s$  is the intrinsic volume density of the particles, which we set to  $1.2 \text{ g cm}^{-3}$ , and  $\Sigma_g$  is the gas surface density.

In our simulations we have the following general setup. We follow the dust evolution from 1000 years up to 1 Myr. We assume a disk around a Solar mass star with an initial disk mass of  $0.05 M_\odot$ . Our radial grid is from 1 to 300 au with 300 cells that are logarithmically spaced. Initially, the gas-to-dust mass ratio is 100 and all the grains are one micron-sized particles. The particle size grid covers up to 2 meters with 180 cells, also logarithmically spaced. The temperature profile is a power-law such that  $T = 160 \text{ K} (r/\text{au})^{-0.5}$ , but we assume a floor value of 10 K, implying that from  $\sim 250$  au the temperature becomes constant. We assume an exponentially tapered power-law function for the initial gas surface density (Lynden-Bell & Pringle 1974)

$$\Sigma_g(r, t_0) = \Sigma_0 \left( \frac{r}{R_c} \right)^{-\gamma} \exp \left[ - \left( \frac{r}{R_c} \right)^{2-\gamma} \right] \quad (2)$$

with  $\gamma = 1$  and a characteristic radius of  $R_c = 80$  au. The gas surface density is viscously evolving following the diffusion equation obtained from the continuity equation and angular momentum conservation of the gas in protoplanetary disks and assuming Keplerian frequency everywhere in the disk (Pringle 1981), i.e.,

$$\frac{\partial \Sigma_g(r, t)}{\partial t} = \frac{3}{r} \frac{\partial}{\partial r} \left[ r^{1/2} \frac{\partial}{\partial r} (\nu \Sigma_g r^{1/2}) \right], \quad (3)$$

where  $\nu$  is the disk kinematic viscosity. We use the parametrization by Shakura & Sunyaev (1973), such that

$$\nu = \alpha c_s h \quad \text{with} \quad h = \frac{c_s}{\Omega}, \quad (4)$$

where  $c_s$  is the isothermal sound speed,  $h$  is the gas pressure scale height, and  $\Omega$  the Keplerian frequency. The parameter  $\alpha$  is assumed to take values that range from  $10^{-5}$  to  $10^{-2}$ , the former being a value expected in the dead zones of protoplanetary disks (Nelson et al. 2013; Klahr & Hubbard 2014; Lyra 2014; Flock et al. 2015, 2020) and the latter being values expected in the magnetorotational instability active regions (e.g. Fromang & Nelson 2006; Davis et al. 2010; Simon et al. 2011; Flock et al. 2012; Turner et al. 2014).

#### 2.1.1. Disentangling the effects of gas diffusion vs. dust (radial and vertical) diffusion

Current dust evolution models of protoplanetary disks assume a dependence of turbulent velocities, vertical stirring, and radial diffusion of dust particles on the parameter  $\alpha$  that regulates the gas viscous evolution. In our simulations, we assume non-isotropic turbulence and thus the parameters that control these physical mechanisms are independent from each other. We use the symbols  $\delta_t$ ,  $\delta_z$ , and  $\delta_r$ , for the turbulence, settling and radial diffusion, respectively. We always assume that particles cannot diffuse faster (radially or vertically) than the gas (i.e.,  $\delta_{r,z,t} \leq \alpha$ ).

**Vertical stirring and settling.** The velocities of very small particles ( $\lesssim 1 \mu\text{m}$  sized grains) are usually dominated by Brownian motion, but this becomes negligible as soon as particles grow to larger sizes (e.g., Birnstiel et al. 2016, see their Fig. 1). From micron to sub-millimeter sized dust grains, settling can be an important source for the velocity of the dust and their collisions. When neglecting the stirring by gas turbulence, the vertical velocity of grains that settle to the midplane ( $v_{z,\text{settling}}$ ) is given by balancing the gas drag force with the vertical gravitational force,  $F_{\text{grav}} = -m\Omega^2 z$ . This gives the terminal velocity for particles coupled to the gas ( $\text{St} < 1$ )  $v_{z,\text{settling}} = -z\Omega\text{St}$  (Safronov 1969; Dullemond & Dominik 2004). This implies that the settling velocity decreases close to the midplane where the gas density increases, and it also increases for particles with higher Stokes number (for  $\text{St} < 1$ ). Nonetheless, particles are also expected to be stirred up above the midplane by vertical turbulence. Vertical and radial turbulence may differ due to different instabilities, such as the Goldreich-Schubert-Fricke instability (Nelson et al. 2013; Stoll & Kley 2014).

The relative velocities between particles due to settling depend on their height above the midplane, and we assume a Gaussian vertical mass distribution for which the scale height depends on the vertical stirring parameter  $\delta_z$ . The particle scale height  $h_d$  is given by (Youdin & Lithwick 2007; Birnstiel et al. 2010)

$$h_d(\text{St}) = h \times \min \left( 1, \sqrt{\frac{\delta_z}{\min(\text{St}, 1/2)(1 + \text{St}^2)}} \right). \quad (5)$$

As demonstrated below, when the relative velocities due to turbulent motion and/or radial drift are low, relative

velocities due to settling can dominate, in which case we use the settling limit obtained in the Appendix A.

Although we do not include the vertical evolution of the particle density distribution, we do calculate the total volume dust density as a function of  $h_d$  and provide these 2D  $(r, z)$  particle density distribution to the radiative transfer models. The volume dust density is assumed to follow

$$\rho_d(r, \varphi, z, St) = \frac{\Sigma_d(r, St)}{\sqrt{2\pi} h_d(r, St)} \exp\left(-\frac{z^2}{2h_d^2(r, St)}\right), \quad (6)$$

where  $z = r \cos(\theta)$ , with  $\theta$  being a polar angle; and  $\Sigma_d$  is the dust surface density.

**Turbulent velocities.** For particles larger than sub-millimeter sizes, turbulence and radial drift can dominate the relative velocities, and both of them depend on the Stokes number. We approximate the turbulent velocities by (Ormel & Cuzzi 2007)

$$v_f^2 \sim 3\delta_t St c_s^2. \quad (7)$$

When assuming that turbulence dominates the relative velocities of particles and that sticking collisions happen below the fragmentation speed  $v_f$ , the maximum grain size  $a_{f, \text{turb}}$  is given by the so-called fragmentation barrier (Birnstiel et al. 2010, 2012)

$$a_{f, \text{turb}} = \frac{2}{3\pi} \frac{\Sigma_g}{\rho_s \delta_t} \frac{v_f^2}{c_s^2}. \quad (8)$$

In this work, we assume values of  $\delta_t$  that are either equal or lower to  $\alpha$ . Physically, this would imply that what sets the gas viscous evolution may be detached from what dominates the turbulent motion of the grains. This is possible for instance in the weakly ionized regions (or dead zones), where MRI is not effective as expected in the dense mid-plane regions, while what drives the gas accretion and the angular momentum transport in the disk may be driven by other and more effective physical mechanism such as a MHD disk wind (e.g., Bai 2016).

Growth can be also limited by radial drift due to the rapid timescale of radial drift. When balancing the growth timescales with the drift timescales (Klahr & Bodenheimer 2006) and assuming relative particle speeds are dominated by turbulent motion, the drift barrier is given by (Birnstiel et al. 2012)

$$a_{\text{drift}} = \frac{2\Sigma_d}{\pi\rho_s} \frac{v_K^2}{c_s^2} \left| \frac{d \ln P}{d \ln r} \right|^{-1}. \quad (9)$$

where  $P$  is the disk gas pressure and  $v_K$  the Keplerian speed.

The two population model presented by Birnstiel et al. (2012) takes advantage of top-heavy size distributions and of the radial drift speed increasing with size (for Stokes numbers below unity). Under these conditions, particle evolution can be simplified by assuming a particle flux dominating large species and a small species that is radially transported mostly via gas motion and particle diffusion.

In the model presented in Birnstiel et al. (2012), it is assumed that fragmentation occurs due to relative turbulent motion or due to relative radial drift. For the drift limit, it is assumed that turbulent motion dominates. However, for low values of  $\delta_t$ , i.e. lower relative turbulent velocities, and/or low particle fragmentation speeds  $v_f$ , the dominating source of relative velocity can switch to relative vertical settling or relative radial drift—both in the fragmentation and drift regime. This means that in each regime either turbulence, settling, radial drift can also dominate, and thus each regime can have up to three different barriers as explained in the Appendix A. These limits can be used to further generalize the two population model presented in Birnstiel et al. (2012), giving more freedom choosing the viscosity parameter of the gas  $\alpha$ , the particle's turbulence parameter  $\delta_t$ , the vertical ( $\delta_z$ ) and radial ( $\delta_r$ ) particle diffusion parameters separately.

**Radial diffusion.** For the dust transport, the advection-diffusion equation of the dust surface density ( $\Sigma_d$ ) is solved for each grain size, given by (e.g. Birnstiel et al. 2010)

$$\frac{\partial \Sigma_d}{\partial t} + \frac{1}{r} \frac{\partial}{\partial r} (r \Sigma_d v_{r,d}) - \frac{1}{r} \frac{\partial}{\partial r} \left[ r \Sigma_g D_d \frac{\partial}{\partial r} \left( \frac{\Sigma_d}{\Sigma_g} \right) \right] = 0, \quad (10)$$

where  $D_d$  is the dust radial diffusivity, which is assumed to be (Youdin & Lithwick 2007)

$$D_d = \frac{\delta_r c_s h}{1 + St^2}. \quad (11)$$

In the classical models,  $\delta_r = \alpha$ , but here we assume independent values with the same motivation than as for  $\delta_t$  or  $\delta_z$ , i.e. the radial diffusion of the grains is independent on the physical mechanism that is responsible of the gas viscous evolution.

### 2.1.2. Combination of $\delta_t$ , $\delta_z$ , $\delta_r$ , and $\alpha$ parameters

Table 1 summarizes the combination of  $\delta_t$ ,  $\delta_z$ ,  $\delta_r$ , and  $\alpha$  that we assume for the models of this paper. Models 1 and 2 are the two extremes in our set of simulations. Model 1 aims to consider a disk where the gas viscous evolution parameter is set to the maximum value ( $10^{-2}$ ) obtained in the active regions of disks from MRI calculations (e.g. Turner et al. 2014), and where the rest of the analyzed parameters have the same values. On the other hand, model 2 is the other extreme where the gas viscous evolution parameter and all the others are set to a very low value expected in a disk where MRI is inefficient ( $10^{-5}$ ). The values for the parameters to explore in models 3 to 9 are such that these cover a transition from the two extremes of model 1 and 2. More specifically, models 7 and 9 also assume that all the four parameters are equal, and the values are  $10^{-3}$  and  $10^{-4}$ , respectively. The rest of the models (#3, 4, 5, 6, and 8) mix different values to resemble different radial/vertical diffusion and/or turbulent velocities of the particles.

### 2.1.3. Inclusion of a pressure bump

We follow the prescription introduced by Dullemond et al. (2018), and also used by Stammerl et al. (2019), to include

**Table 1.** Summary of the models and results without pressure bumps (Fig. 2) Columns 2, 3, 4, 5 show the values taken for the parameters that regulate the gas viscous evolution ( $\alpha$ ), radial diffusion ( $\delta_r$ ), turbulent mixing ( $\delta_t$ ), and vertical settling/stirring ( $\delta_z$ ), respectively. Column 6 shows a  $\checkmark$  mark when pebbles ( $a > 1$  mm) have formed in most of the disk, or a  $\times$  mark otherwise. Column 7 summarizes the relative velocity that sets the maximum grain size, which is always in the fragmentation regime at 1 Myr of evolution. Columns 8 and 9 show the synthetic millimeter fluxes at 1.3 mm and 3.0 mm, respectively. Column 10 is the spectral index. Columns 11 and 12 show the dust radius that encloses 68% or 90% of the 1.3 mm flux.

(1) Model	(2) $\alpha$	(3) $\delta_r$	(4) $\delta_t$	(5) $\delta_z$	(6) Pebble formation? ( $a > 1$ mm)	(7) $a_{\max}$ set by:	(8) $F_{1.3\text{mm}}$ [mJy]	(9) $F_{3.0\text{mm}}$ [mJy]	(10) $\alpha_{\text{mm}}$	(11) $R_{\text{dust},68\%}$ [au]	(12) $R_{\text{dust},90\%}$ [au]
1	$10^{-2}$	$10^{-2}$	$10^{-2}$	$10^{-2}$	$\times$	turbulence	127.2	6.0	3.7	120	257
2	$10^{-5}$	$10^{-5}$	$10^{-5}$	$10^{-5}$	$\checkmark$	drift	295.2	19.3	3.3	57	91
3	$10^{-2}$	$10^{-2}$	$10^{-4}$	$10^{-3}$	$\checkmark$	settling/drift	198.4	10.3	3.5	41	82
4	$10^{-2}$	$10^{-2}$	$10^{-5}$	$10^{-2}$	$\times$	settling	163.4	7.3	3.7	55	198
5	$10^{-2}$	$10^{-3}$	$10^{-5}$	$10^{-2}$	$\times$	settling	150.4	7.0	3.7	37	95
6	$10^{-3}$	$10^{-3}$	$10^{-5}$	$10^{-3}$	$\checkmark$	settling/drift	295.5	21.2	3.2	58	87
7	$10^{-3}$	$10^{-3}$	$10^{-3}$	$10^{-3}$	$\times$	turbulence	313.6	17.0	3.5	47	91
8	$10^{-3}$	$10^{-4}$	$10^{-5}$	$10^{-4}$	$\checkmark$	drift	304.2	19.2	3.3	65	96
9	$10^{-4}$	$10^{-4}$	$10^{-4}$	$10^{-4}$	$\checkmark$	turbulence/drift	327.9	22.3	3.2	61	95

a pressure bump in the disk. This assumes a bump that originates from variations of the viscosity parameter ( $\alpha$ ), modeled as

$$\alpha'(r) = \frac{\alpha}{F(r)}, \quad (12)$$

where  $F(r)$  is given by

$$F(r) = \exp \left[ -f \exp \left( -\frac{(r - r_p)^2}{2w_{\text{gap}}^2} \right) \right]. \quad (13)$$

From previous inspections of the results of the models without bumps, we performed six simulations with this pressure bump as summarized in Table 2. In these models, only  $\alpha$  varies with radius, and the rest of the other parameters are set as before for comparison (see Table 2, for more details). We assume the position of the bump at  $r_p = 40$  au, with an amplitude of  $f = 2$  (as in Dullemond et al. 2018; Stammler et al. 2019), and a width of  $w_{\text{gap}} = 5$  au, which is approximately two times the local pressure scale height at  $r_p = 40$  au. However, the pressure bump itself forms further out, around  $\sim 52$  au where the pressure scale height is  $\sim 3.5$  au.

## 2.2. Radiative transfer calculations

To compute synthetic images and spectral energy distributions (SEDs) for each model. We consider the resulting vertical particle distribution (Eq. (6)) after 1 Myr of evolution as an input to the radiative transfer calculations, for which we use RADMC-3D (Dullemond et al. 2012). We calculate the opacity of each grain size considering porous spheres with a dust mixture composed of astronomical silicates (Draine 2003), carbonaceous material (Zubko et al. 1996), and water ice Warren & Brandt (2008), as in Ricci et al. (2010). We assume a blackbody radiation field from

the central star as the the radiation source and use  $1 \times 10^7$  photons for our calculations.

We obtain the temperature profile for each grain size and calculate scattered light images at 1.25  $\mu\text{m}$  and 1.3 mm. We assume a disk inclination of  $20^\circ$ , a position angle of zero, and a distance to the source of 140 pc as the typical distances to nearby star-forming regions, such as Lupus, Taurus, and Ophiuchus. The synthetic scattered light images are computed including the full treatment of anisotropic scattering with polarization as in Kataoka et al. (2015) and Pohl et al. (2016). Afterwards, the images are convolved by a Gaussian point-spread-function (with a size of  $0.04'' \times 0.04''$ ), at the two wavelengths, which is similar to the angular resolution that is currently possible to obtain with SPHERE/VLT and ALMA telescopes. The intensity profiles created at 1.25  $\mu\text{m}$  are then multiplied with the square of its distance to the star to compensate for the stellar illumination. From the intensity profiles at 1.3 mm we calculate the radius that enclosed either 68% or 90% of the emission by assuming that the sensitivity of the observations provide a signal-to-noise ratio with respect to the maximum of the emission (peak) of 1000.

## 3. Results

### 3.1. Models without pressure bumps

The particle density distribution as a function of distance from the star and grain size of the models without any pressure bump (Table 1) are shown in Fig. 2. The white solid line represents particles with  $\text{St} = 1$ , the cyan and red lines represent the fragmentation (Eq. (A.17)) or drift (Eq. (A.32)) regime, respectively. The style of the lines shows what dominates the relative velocity: turbulence, radial drift, or settling. We do not include in this figure the turbulence I regime or the azimuthal drift since they do not dominate the relative velocities in any case at the shown snapshot (see Appendix A). The horizontal gray line shows  $a = 1$  mm and we call pebbles particles bigger than this size. All panels show the results at 1 Myr of evolution (as

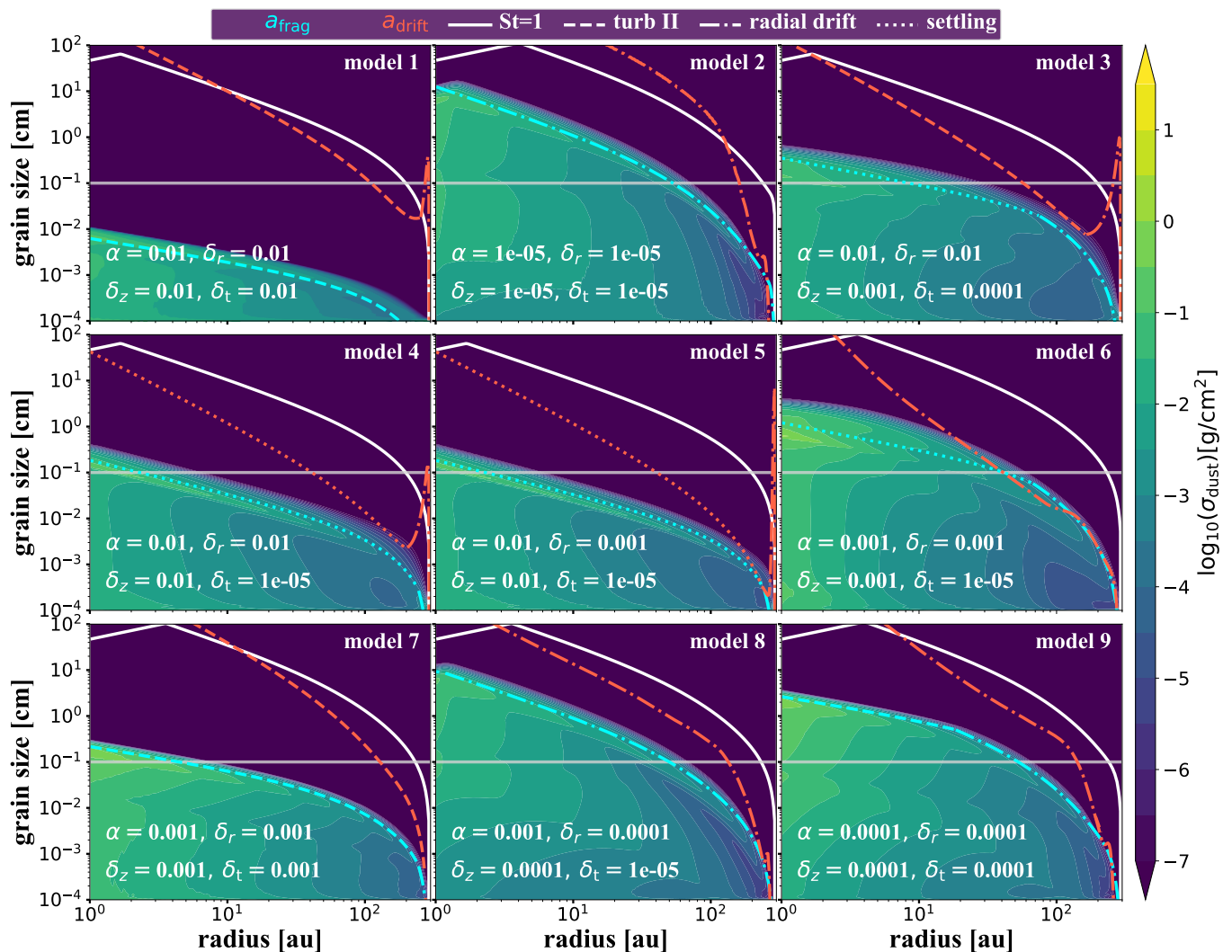


**Fig. 2.** Particle density distribution after 1 Myr of evolution as a function of distance from the star and grain size of the models without any pressure bump (Table 1). The white solid line represents a Stokes number of unity. The cyan and red colors are used to show the fragmentation (Eq. (A.17)) and drift (Eq. (A.32)) limit. The style of the line shows what dominates the relative velocity: turbulence (Eqns. (A.16) and (A.27)), radial drift (Eqns. (A.10) and (A.24)), and settling (Eqns. (A.15) and (A.25)). We do not include the turbulence I regime or the azimuthal drift since they do not dominate the relative velocities in any case for the shown snapshot. The horizontal gray line shows  $a = 1$  mm and we call pebbles particles bigger than this size.

the typical age of class II protoplanetary disks in nearby star forming regions like Taurus and Lupus) and in all cases the fragmentation speed is  $v_f = 1 \text{ m s}^{-1}$ .

Model 1 and 2 are the two extremes of our assumptions, where model 1 has for all the parameters that set the gas and dust diffusion as well as relative turbulent speeds the same value of  $10^{-2}$  and model 2 corresponds to the case of  $10^{-5}$ . As expected in model 1, pebble ( $a > 1$  mm) formation does not happen. The maximum grain size in the case of model 1 is set by high velocities due to turbulence inducing the fragmentation barrier ( $a_{f,\text{turb}}$ , Eq. 8) and the maximum grain size is approximately 0.01 cm at 1 au and around  $10 \mu\text{m}$  in the outer part of the disk (at around 100 au). On the other hand, model 2 allows the formation of pebbles in most of the disk where the maximum grain size is set by fragmentation where the radial drift velocities dominate.

The results of model 1 and 2 are not surprising since  $a_{f,\text{turb}}$  depends quadratically on the fragmentation velocity, so if we assume a fragmentation velocity that is one order of magnitude lower than previously used, theory requires

us to decrease the dust turbulence by at least two orders of magnitude, if turbulence is the main source of relative velocities. Model 9 is as model 2 but with  $10^{-4}$ , where it is possible to see that the maximum grain size for  $r < 50$  au is set by fragmentation by turbulence and by drift in the outer regions. In this case there is still some pebble formation. While model 7 assumes all gas and dust diffusion parameters to be equal to  $10^{-3}$  and pebble formation does not happen in most of the disk as in model 1. So the first conclusion of these numerical experiments is that with isotropic turbulence and  $v_f = 1 \text{ m s}^{-1}$ , pebble formation can happen in disks when the gas and dust diffusion is low, with values of  $10^{-5} - 10^{-4}$ .

However, the main motivation of the other experiments of this work are: first, when  $\alpha$  has values of  $10^{-5} - 10^{-4}$  the disk accretion rate at million years time scales are expected to be  $10^{-12} - 10^{-11} M_\odot \text{ yr}^{-1}$ , which is much lower than the typical accretion rates in different star forming regions of different age (1-10 Myr, see e.g., Manara et al. 2020). For values of  $\alpha$  of  $10^{-3} - 10^{-2}$ , the accretion rates values

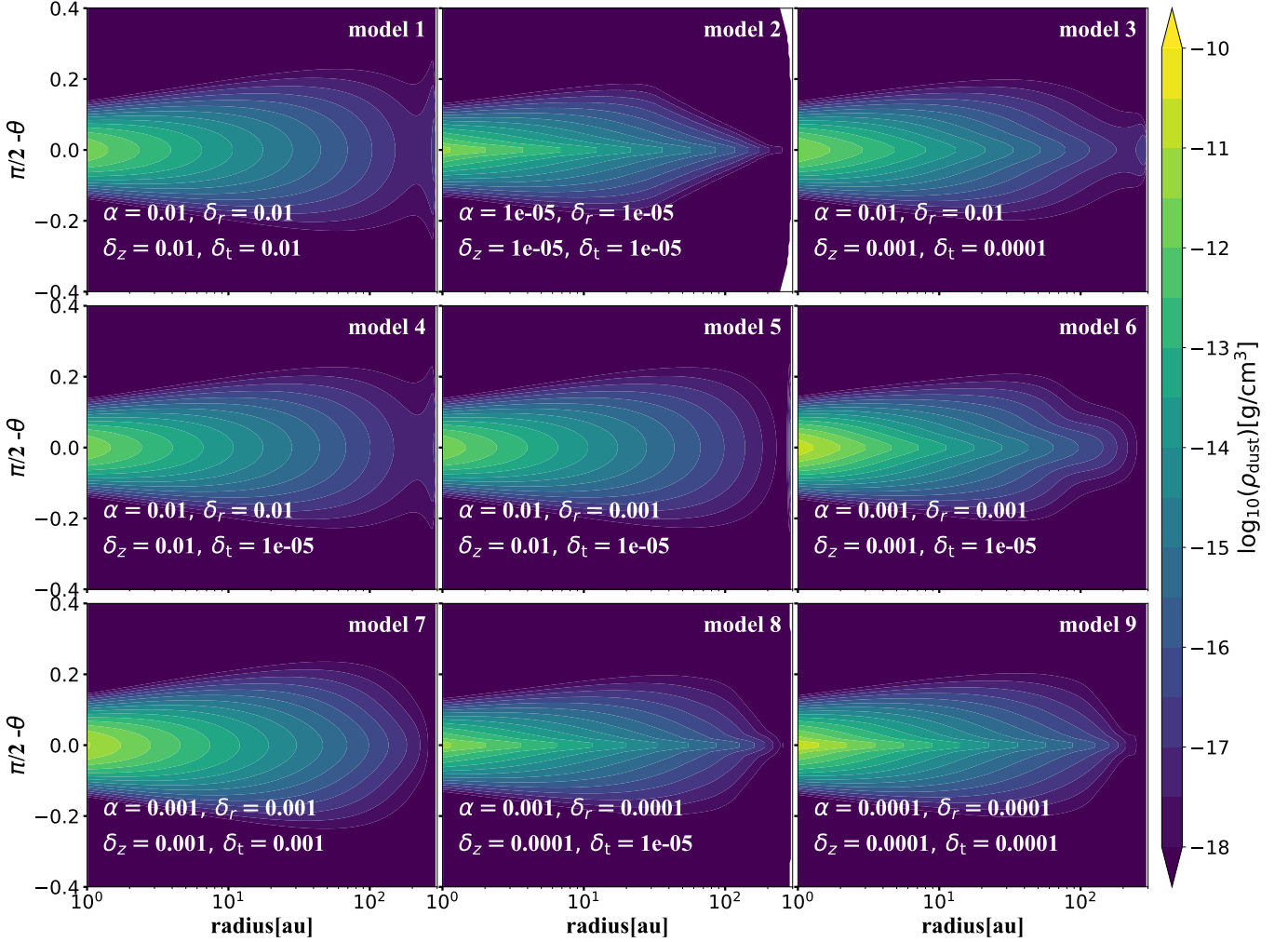


**Fig. 3.** Vertical and radial particle density distribution for all grain sizes of the models without any bumps after 1 Myr of evolution.

are in agreement with the mean values from observations (i.e.,  $10^{-9} - 10^{-10} M_{\odot} \text{ yr}^{-1}$ ). So in the rest of the numerical experiments we keep  $\alpha = 10^{-2}$  or  $\alpha = 10^{-3}$ , and vary the parameters responsible for the radial and vertical particle diffusion as well as the parameter controlling the collision speed due to turbulent motion.

The second motivation of these numerical experiments is that several protoplanetary disks appear to be flared when observed in scattered light (Avenhaus et al. 2018). Assuming that we trace micron-sized particles with these observations, and taking values of  $\delta_z = 10^{-5} - 10^{-4}$ , micron-sized particles would be mainly settled to the midplane, contradicting observations. The third motivation is that the width of some rings in protoplanetary disks observed at very high resolution with ALMA have been resolved (e.g., Dullemond et al. 2018, with values of 4-20 au) and therefore there must be a radial diffusion inside pressure bumps to widen the distribution of millimeter-sized particles, otherwise all the observed rings would be “infinitely” narrow (dust grains would move to the location of the pressure maximum).

Our models 3, 4, 5, and 6 aim to keep high values of  $\alpha$ ,  $\delta_r$ , and  $\delta_z$  to guarantee accretion rate values, width of rings, and dust aspect ratios that are in accordance with observations, while the parameter that control the turbulent velocities ( $\delta_t$ ) of the particles is low. Model 8 is an experiment where we also decrease  $\delta_z$  to  $10^{-4}$  since by previous

inspections of the models, we notice that settling can set the maximum grain size and limit the formation of pebbles. Table 1 summarizes if pebble formation happens in our models and what sets the maximum grain size in each case. Note that at 1 Myr of evolution all the cases are in the fragmentation regime, but the relative velocity that dominates and sets the maximum grain size is different.

From our numerical experiments where we used different values for  $\delta_t$ ,  $\delta_z$ ,  $\delta_r$ , and  $\alpha$  (i.e., models 3, 4, 5, 6, and 8), the maximum grain size is set either by settling or radial drift. In models 4 and 5 pebble formation is not possible almost in the entire disk ( $r > 2$  au) when  $\delta_z = 10^{-2}$ , this is because the average settling velocities dominate the total relative velocities and set the maximum grain size. Models 4 and 5 are identical except for the radial diffusion, which is lower in model 5. This creates a small effect in the particle distribution, but it can be seen that the radial extension of the large grains is slightly bigger for model 4, as we will discuss in the Sect. 4 when we compare with observations.

For models 3 and 6 with  $\delta_z = 10^{-3}$ , the maximum grain size is mostly set by settling and only in the very outer regions is set by drift. In these two cases, pebble formation happens for  $r < 10$  au in model 3 and for  $r < 50$  au for model 6. Model 6 produces pebbles in a large range of the disk and it is a good compromise when comparing with observations, i.e. an  $\alpha = 10^{-3}$  that gives accretion rates

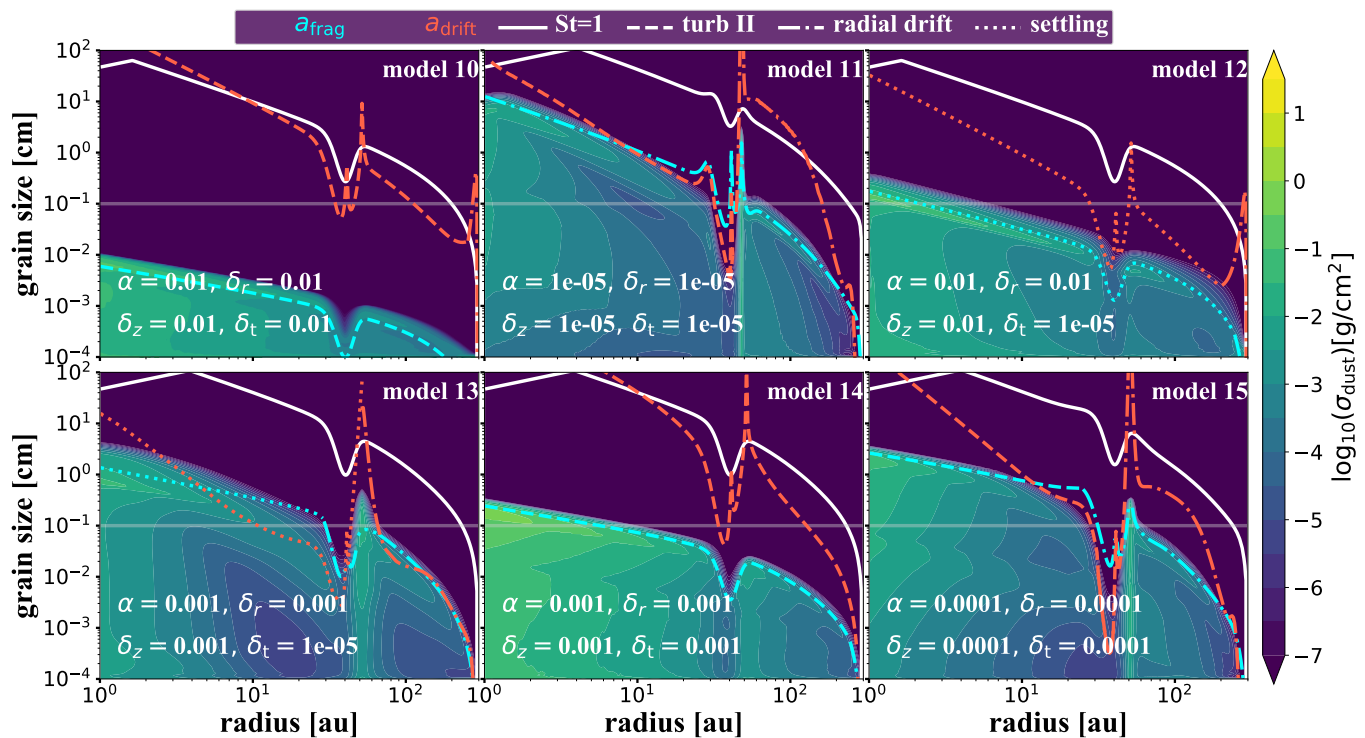


**Fig. 4.** Particle density distribution of the models with a pressure bump in the outer part of the disk (dip located at 40 au) after 1 Myr of evolution. We follow the same procedure than Fig. 2 for the barriers.

of  $10^{-9} M_{\odot} \text{yr}^{-1}$ , a  $\delta_z = 10^{-3}$  that can lead to enough vertical stirring to have a large dust aspect ratio similar to the ones observed with SPHERE for T-Tauri and Herbig disks, and a  $\delta_r$  that can lead to radial diffusion and a wider distribution of pebbles (also under the potential presence of a pressure bump).

There is not a direct observational constraint that can help us to fix  $\delta_t$ . Indirect measurements of the disk turbulence have been done using ALMA observations by searching for variations from Keplerian motion of the gas emission that may come from turbulence (Flaherty et al. 2015, 2017, 2020; Teague et al. 2016, 2018). These works found low values of turbulence for most (but not all) of the disks ( $\lesssim 10^{-3}$ ). In fact, as shown in Flaherty et al. (2020), DM Tau is the only system observed so far with high turbulence.

Figure 3 shows the 2D (radial and vertical) particle density distribution assumed for the radiative transfer calculations and obtained using Eq. (6). We show the vertical and radial particle density distribution considering all the grain sizes. The biggest difference is seen between our two extremes model 1 ( $\alpha, \delta_{r,z,t} = 10^{-2}$ ) and model 2 ( $\alpha, \delta_{r,z,t} = 10^{-5}$ ), where it is clear that in model 2 there is much less stirring of dust particles from the midplane making the dusty disk thinner. Another clear result from Fig. 3 is that when the maximum grain size is set by the fragmentation limit due to radial drift, the disk becomes thinner in all grains. This happens in all the disk for models 2 and 8 where the radial drift dominates the relative velocities everywhere, and from the location where the barrier is set by radial drift and outwards for models 3, 6, and 9. In addition, in the models where  $\delta_z \leq 10^{-4}$  (models 2, 3, 8, and 9), the particle density distribution is much more dominated by the midplane compared to the other models.

### 3.2. Models with a pressure bump in the outer disk

We chose our two extreme cases (model 1 and 2) for the inclusion of a pressure bump, together with the other two cases where all the gas and dust diffusion parameters are constant (model 7 and 9). In addition to these cases, we included 2 more cases, one where the maximum grain size is set by settling in the whole disk (model 4). The other case that we considered is model 6, where pebble formation occurs and the maximum grain size is set by a mix of settling and drift. The summary of the models that include a pressure bump as described in Eqns. (12) and (13) is in Table 2.

The particle density distribution as a function of distance from the star and grain size for the case of a gap at 40 au and a pressure bump at the edge of that gap is shown in Fig 4. Note that because this gap is formed in the  $\alpha$  viscosity, any variation of the value of  $\alpha$  changes the timescale in which this gap and bump is formed. Because all the plots are shown at 1 Myr, in model 11 when  $\alpha$  is the lowest, the gap is still opening and the amplitude of the bump is the lowest. The gap is also shallower for model 15 ( $\alpha = 10^{-4}$ ) compared to the rest of the models.

There is effective trapping, reflected by the significant particle accumulation at the pressure maximum, in the cases where there is pebble formation (models 11, 13, and 15). In the other cases, the strong radial mixing (both via the radial particle diffusion parameter and the radial gas velocity by which small particles are dragged along) does not lead to significant trapping and hence no significant accumulation of particles at the pressure maximum (models 10, 12, and 14).

Note that in the case that there is no efficient trapping (models 10, 12 and 14), there is anyway a small decrease on the maximum particle size at the location of the gap, be-

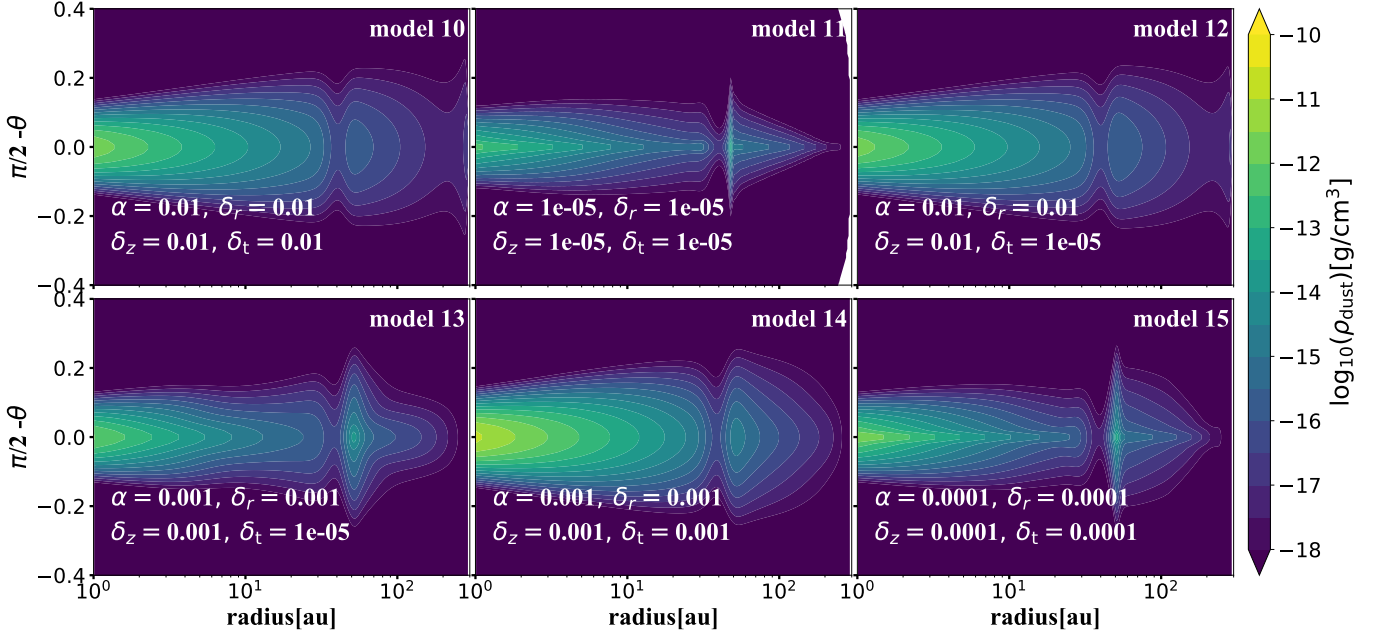


**Fig. 5.** Vertical and radial particle density distribution of all grain sizes of the models with a pressure bump located in the outer disk.

**Table 2.** Summary of the models and results with a pressure bump (Fig. 4). In Column 3 a  $\checkmark$  mark is given when efficient trapping happens in the pressure bump, otherwise a  $\times$  mark is shown.

(1) Model	(2) Description	(3) Trapping?	(4) $F_{1.3\text{mm}}$ [mJy]	(5) $F_{3.0\text{mm}}$ [mJy]	(6) $\alpha_{\text{mm}}$	(7) $R_{\text{dust},68\%}$ [au]	(8) $R_{\text{dust},90\%}$ [au]
10	as model 1 with bump	$\times$	119.4	5.7	3.6	141	263
11	as model 2 with bump	$\checkmark$	203.8	12.4	3.3	75	100
12	as model 4 with bump	$\times$	148.8	6.8	3.7	78	213
13	as model 6 with bump	$\checkmark$	331.2	24.1	3.1	65	88
14	as model 7 with bump	$\times$	286.6	16.8	3.4	61	97
15	as model 9 with bump	$\checkmark$	247.7	16.0	3.3	73	101

cause the fragmentation barrier is proportional to the gas surface density (either when is set by turbulence or settling). In the case that there is not trapping and the maximum grain size is set by settling (model 12), the decrease in particle size at the gap location is smaller.

In the cases of effective particle trapping, model 11 ( $\alpha, \delta_{r,z,t} = 10^{-5}$ ) shows a situation where grain growth is very efficient in the pressure maximum and particles grow to the maximum size that is allowed in our grid (2 m) at that location. This is because the relative velocity that dominates for the fragmentation is radial drift, which is zero at pressure maximum. This has been seen before in simulations with particle traps and low turbulence and diffusion of the grains (e.g. Pinilla et al. 2015). Models 13 ( $\alpha, \delta_{r,z} = 10^{-3}$ , and  $\delta_t = 10^{-5}$ ) and 15 ( $\alpha, \delta_{r,z,t} = 10^{-4}$ ) where effective trapping happens, settling or turbulence sets the maximum grain size inside the pressure bump, respectively. Note that the width of the dust accumulation inside the gap decreases for lower  $\delta_r$ , i.e., model 11 ( $\delta_r = 10^{-5}$ ) shows the narrowest accumulation, followed by model 15 ( $\delta_r = 10^{-4}$ ), and then by model 13 ( $\delta_r = 10^{-3}$ ).

Figure 5 shows the vertical and radial distribution integrated over all the grain sizes for each model that include a pressure bump. In the cases where there is no efficient dust

trapping (model 10, 12, and 14) there is a small decrease of the particle density distribution that is more evident in the upper layers of the disk, but it is still noticeable at the midplane.

In the cases with effective trapping (model 11, 13, and 15), the depletion of grains extends from the surface layers down to the midplane, especially in case 11 and 15 where the radial diffusion and vertical stirring are low. At the location of the trap, there is clear increase of small grains due to continuous fragmentation of dust particles, as seen before in e.g. Pinilla et al. (2012) and Pinilla et al. (2015), but also in 2D dust evolution simulations by Drażkowska et al. (2019). Due to this local increase of the small particles, there is an increase of their vertical distribution due to vertical stirring. This is more clear in model 13 and model 15 where the vertical stirring parameter is higher than in model 11. Model 13 is the case with more radial diffusion and this is why there is a significant amount of grains present throughout the gap, more than in model 11 or 15.

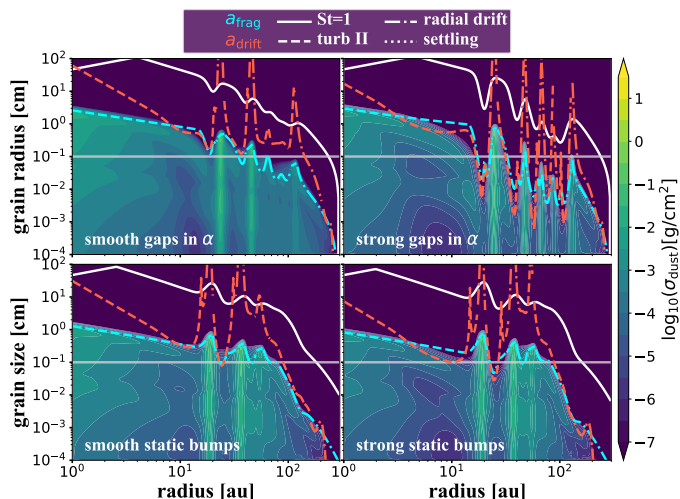


**Fig. 6.** As Fig. 2 but with multiple pressure bumps induced either by variations in  $\alpha$  and with different depth of the gaps (top panels), or introduced in the gas surface density that remains constant over time (bottom panels). The growth barriers follow the same convention than Fig. 2. In these cases,  $\alpha, \delta_{r,z,t} = 10^{-4}$  for all four simulations.

## 4. Discussion

### 4.1. Millimeter fluxes and spectral indices

Tables 1 and 2 provide the expected millimeter fluxes at 1.3 mm (ALMA Band 6) and 3.0 mm (ALMA Band 3) after taking the particle density distribution after 1 Myr of evolution and then use radiative transfer simulations to create the SEDs.

Model 1, where the fragmentation barrier is the lowest and where pebble formation does not happen in the disk, is the case with the lowest millimeter fluxes. In general, the cases where pebbles are not formed or they are formed in just a small region of the disk have the lower millimeter fluxes, except for model 7, where all the gas and dust diffusion parameters are set to  $10^{-3}$ . For all the cases, there is no correlation between the velocities that set the maximum grain size and the obtained fluxes. All of the fluxes are within the observed values of the disks in different star forming regions around T-Tauri and Herbig stars (e.g., Ricci et al. 2012; Tripathi et al. 2017; Andrews et al. 2018b).

When comparing the models with and without a bump in the disk, in all of the cases (except for model 6 vs. model 13), the millimeter fluxes decrease when including the bump. In the case that trapping happens this originates from: (i) grains growing to decimeter objects, which have very low opacities and contributing very little to the total fluxes (model 2 vs. model 11), or/and (ii) the emission inside the trap becoming optically thick (as in the case of model 15). In model 13 (model 6 but with a bump), grains in the trap have a maximum size of  $\sim 1$  cm and the emission is optically thin such that the millimeter fluxes slightly increase with the trapping, as expected since less grains are drifting towards the star. In the cases without efficient trapping, the fluxes decrease when compared to the same without a bump. In all these cases, we have a local decrease of the maximum grain size at the gap location, which helps to decrease the total millimeter flux.

For all the models, we obtain the millimeter spectral index ( $\alpha_{\text{mm}}$ ) taking the fluxes at 1.3 mm and 3.0 mm, such that  $\alpha_{\text{mm}} = \log_{10}(F_{1.3\text{mm}}/F_{3.0\text{mm}})/\log_{10}(3.0/1.3)$ . All the spectral indices in our work are much higher than observed (e.g., Ricci et al. 2012; Pinilla et al. 2017b). As shown in Pinilla et al. (2012), high spectral indices from dust evolution models are expected when radial drift is included. Even when pebble formation occurs and the millimeter fluxes are in agreement with observations, the amount of pebbles is not enough to have low spectral indices. Even in the case of models with effective trapping, the values of the spectral index remain similar as in models without a bump, implying that this bump does not maintain enough pebbles to decrease the values of the spectral index (in fact only 1-2% of the total dust mass is in pebbles). To solve the discrepancy strong multiple bumps can assist to decrease  $\alpha_{\text{mm}}$  (Pinilla et al. 2012), or if only one single bump is included, it has to be strong enough as the one expected from a giant planet to decrease the spectral index (Pinilla et al. 2014). In this case, the spectral index depends where the bump is located becoming larger when the bump is located further out. Another factor that can influence the final spectral indices is the lifetime of the pressure bumps, since in previous works (e.g. Pinilla et al. 2012, 2013, 2014), pressure bumps are included from the beginning of the simulation and they are static, while in the present work the gap and bump is growing with viscous timescales. Considering completely static bumps or bumps that slowly grow with time have both their limitations. A prescription of a bump in  $\alpha$  allows to have mass accretion onto the star as well as viscous spreading, however, for very low values of  $\alpha$  it can take more than 1 Myr to reach the final amplitude of the bump, which may not be the case of e.g. planets being responsible for the bump formation. A more realistic approach would include the viscous evolution and the grow, appearance and disappearance of a number of bumps with a given frequency during the disk lifetime.

To test if multiple gaps as assumed in this paper vs. static multiple bumps have an influence on the spectral index, we performed 4 more models considering the  $\alpha$  and  $\delta_{r,z,t}$  from model 9 (i.e.,  $\alpha, \delta_{r,z,t} = 10^{-4}$ ) and we took 5 gaps or bumps with the same width of 2 local pressure scale heights, and they are located at 20, 40, 60, 80 and 100 au, specifically:

- A model with 5 gaps as prescribed in this paper (Eq. 12 and Eq. 13) with  $f = 2$  (name: smooth gaps in  $\alpha$ ).
- As the previous model, but with  $f = 4$  (name: strong gaps in  $\alpha$ ).
- A model with 5 bumps as described in Pinilla et al. (2020), which are introduced as perturbations in the initial gas surface density profile and they remain static. Specifically,

$$\Sigma'_g(r) = \Sigma_g(r) \times \left[ 1 + \sum_i B_i \right], \quad (14)$$

with

$$B_i(r) = A_i \exp\left(-\frac{(r - r_{p,i})^2}{2w_i^2}\right) \quad (15)$$

The locations ( $r_{p,i}$ ) of these perturbations are 20, 40, 60, 80 and 100 au, and the width ( $w_i$ ) of each of them

is two local pressure scale heights. The amplitude ( $A_i$ ) for all is 2 (name: smooth static bumps).

- As the previous one but with an amplitude of 4 (name: strong static bumps).

The results of these tests are summarized in Fig 6, which shows the particle density distribution at 1 Myr of evolution. It is important to note that in the case where the perturbations are introduced in the gas surface density (Eq. 14), the bumps are located at the position where the gaps are in the other two cases. In addition, in the cases of static bumps, the perturbations overlap in the outer part of the disk, which leads to less effective number of bumps.

After taking these dust density distributions and performed the radiative transfer calculations, the spectral index for the models where the gaps are introduced in  $\alpha$  is 2.8, while for the case where the bumps are introduced in the gas surface density and remain static during the dust evolution is 2.5. The last values are similar to the observed values in different disks in several star-forming regions.

These results show that the inclusion of more bumps help to decrease the spectral index and the fact that they live from the starting point of the simulations with a given amplitude decreases the values of the spectral index to the averaged values that have been observed. Since the bumps formed by variations of  $\alpha$  evolve on viscous times scales, if these times are larger than the growth timescale, it is expected less trapping than static pressure bumps. The amplitude here does not seem to play an important role, probably because with these prescription of the bumps and gaps, there is not full filtration or in other words radial mixing still allows the grains to move out of the pressure bumps, but deeper investigation is required to confirm this.

#### 4.2. Dust disk radii

Using the intensity profile obtained from the synthetic maps at 1.3 mm, we calculate the radius that enclosed either 68% ( $R_{\text{dust},68\%}$ ) or 90% ( $R_{\text{dust},90\%}$ ) of the emission by assuming a signal-to-noise ratio (SNR) with respect to the maximum of the emission of 1000 in all cases. We decided to have a SNR compared to the peak instead of a constant SNR for all of the cases, since most of the observations available with ALMA have different sensitivity, all depending on what is the total flux of each disk and the goal of the observations. Currently, this signal to noise is possible to obtain for the bright disks with ALMA with short (some minutes) integration time. But this SNR is very challenging to achieve for faint disks, and therefore the following discussion is valid when comparing observations with similar SNR with respect to the peak. Tables 1 and 2 include these two dust radii for each simulation.

Our models without pressure bumps (except for model 1) span a large range of values that are in agreement with the values in different star forming regions, such as Ophiuchus, Taurus, and Lupus (Hendler et al. 2020). The mean value of  $R_{\text{dust},68\%}$  in these models (excluding model 1) is  $\sim 53$  au. In these models, the larger disks are also brighter. Our results demonstrate that a combination of gas and dust diffusion parameters can lead to very different particle density distributions, which influences directly the dust outer radius as obtained from millimeter observations.

Model 1 is an outlier where the flux is the minimum that we found, but this is the largest disk according to our models. This is a consequence of the high turbulence and radial diffusion, since the high turbulence produce small grains that are easier to radially diffuse. However, this is the model with the lowest millimeter flux as well, meaning that we would need deeper observations to detect such outer radius. This result would imply that disks can appear large when observed at millimeter emission without the need of any pressure bump. Recent ALMA observations suggest that the large disks remain bright thanks to the presence of substructures, and so far most of the small disks seem to be faint (Long et al. 2019). Current observations open the question of whether or not is the absence of structures the reason for the small and faint disks. The current data have some observational bias, since deeper observations are needed to determine the outer radius of fainter disks and higher resolution is required to detect structures in the very small disks.

The effect of radial diffusion can be more clearly seen when comparing model 4 and model 5, where the only parameter that is different between these two models is  $\delta_r$ . Model 5 has a  $\delta_r$  that is one order of magnitude lower and the disk appears to be smaller, both in the  $R_{\text{dust},68\%}$  and  $R_{\text{dust},90\%}$ , with a higher difference when comparing  $R_{\text{dust},90\%}$  that is twice as high for the disk with the higher radial diffusion (198 au for model 4 vs. 95 au for model 5). In these two models, the flux is very similar and therefore this result is independent of the SNR of the real observations.

In our simulations without pressure bumps,  $R_{\text{dust},90\%}$  can be 1.5 to 3.6 larger than  $R_{\text{dust},68\%}$ , but this strongly depends on the assumption of the SNR. For instance, when assuming half of the signal to noise ratio of our calculations, the  $R_{\text{dust},68\%}$  remains similar (variations within 5 au), while  $R_{\text{dust},90\%}$  decreases such that the  $R_{\text{dust},90\%}$  can be only up 2 times  $R_{\text{dust},68\%}$ .

When comparing models with and without a pressure bump, the dust radii increase for models with a bump, and this increase becomes higher when trapping is efficient (model 11, 13, and 15). The pressure bump is located at  $\sim 52$  au in all the models, and the outer radius is larger than this position, either  $R_{\text{dust},68\%}$  or  $R_{\text{dust},90\%}$ . Pinilla et al. (2020) showed that in the case of strong and static pressure bumps, the outer radius should trace the location of the furthest pressure bump in the disk. In this case, we do not see this trend, which is probably due to the nature of the pressure bump, which in this work is developing with the gas viscous evolution and it has a lower amplitude than in the models by Pinilla et al. (2020). The only model where the outer dust radius does not increase is for model 6, which could be the result of the high radial diffusion when compared to the other two cases where there is trapping.

#### 4.3. Substructures

Figure 7 shows the radial intensity profile of the synthetic images (previously convolved with a Gaussian beam with an FWHM of  $0''.04$  in each case) after radiative transfer calculations assuming the particle density distributions without any pressure bumps from Fig. 3. The intensity profiles are obtained at  $1.25 \mu\text{m}$  and  $1.3 \text{ mm}$ . The intensity profile at  $1.25 \mu\text{m}$  is multiplied by  $r^2$  to compensate by the stellar irradiation. The grey region shows the typical size of

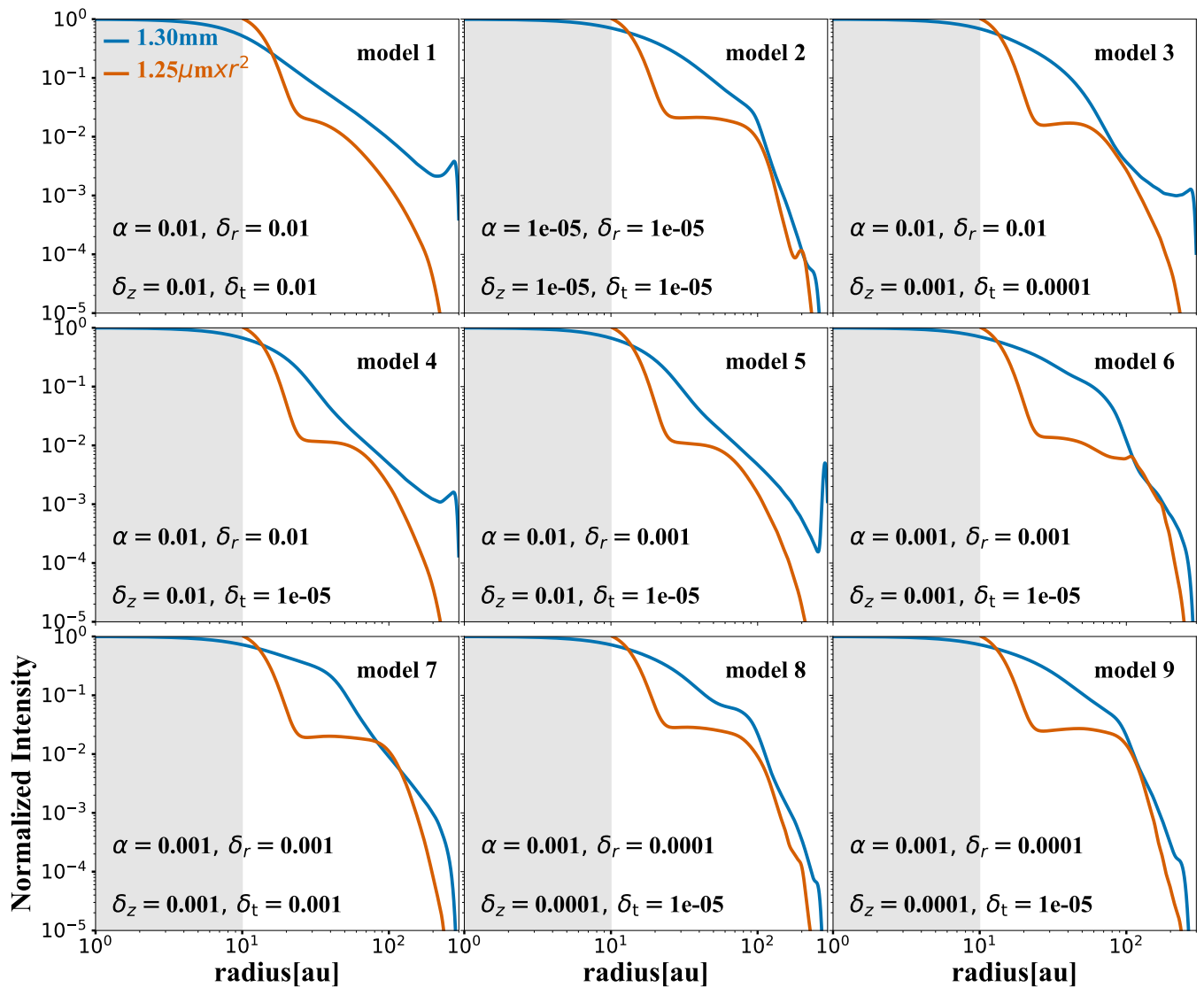


**Fig. 7.** Radial intensity profile of the synthetic images (previously convolved with a Gaussian with an FWHM of  $0''.04$  in each case) after radiative transfer calculations assuming the particle density distributions from Fig. 3. The intensity profiles are obtained at 1.25  $\mu\text{m}$  and 1.3 mm. The intensity profile at 1.25  $\mu\text{m}$  is multiplied by  $r^2$  to compensate the stellar irradiation. The grey regions show the typical size of a coronagraph or/and saturated inner pixels from typical observations at scattered light. Case of models without bumps.

a coronagraph or/and saturated inner pixels from typical observations at scattered light.

All the radial profiles of the intensity at 1.25  $\mu\text{m}$  show a large gap as shown by Birnstiel et al. (2015), even in the absence of any perturbation in the disk or pressure bump. This gap in scattered light originates from the removal of small grains by sweep-up collisions with the large particles. For this gap to form, there must be an equilibrium between vertical settling/stirring and drift, such that the large grains that are drifting inwards would be able to sweep-up the small grains in the disk surface. This gap forms in all our models, and the minimum of this gap is located around  $\sim 25$  au for all the cases. For most of the simulations, the width of the gap (extend up to  $\sim 60$ -80 au) and its contrast (a factor of 10) are similar. Model 1 is the model with the narrower and lowest contrast gap, while model 6 has the widest gap in our simulations (up to  $\sim 100$  au). In Birnstiel et al. (2015), there is a description on where this gap is expected based on the assumptions of the models.

The intensity at 1.3 mm of the synthetic observations of the models without any pressure bumps decreases smoothly with radius for all the models. In some cases, there is a local increase of the intensity close to the outer radial edge of our simulations. This structure should be taken with caution because it is an effect of assuming a floor value of 10 K for the temperature profile from  $\sim 250$  au. Due to this assumption the radial profile of the pressure gradient becomes less steep and there is a local enhancement of the dust large particles. The radial profiles resemble a smooth decrease in the inner parts together with a sharp decrease in the outer disk. Similar to the dust disk radii discussed in Sect 4.2, the location where the transition from a smooth and sharp profile happens depends on the gas surface density profile and how its vacuously spreading outwards, the particle size, and on all the dust diffusion parameters that are involved, as discussed in Birnstiel & Andrews (2014).

For the models with a bump and in the cases without effective trapping (models 10, 12, and 14), there is a gap

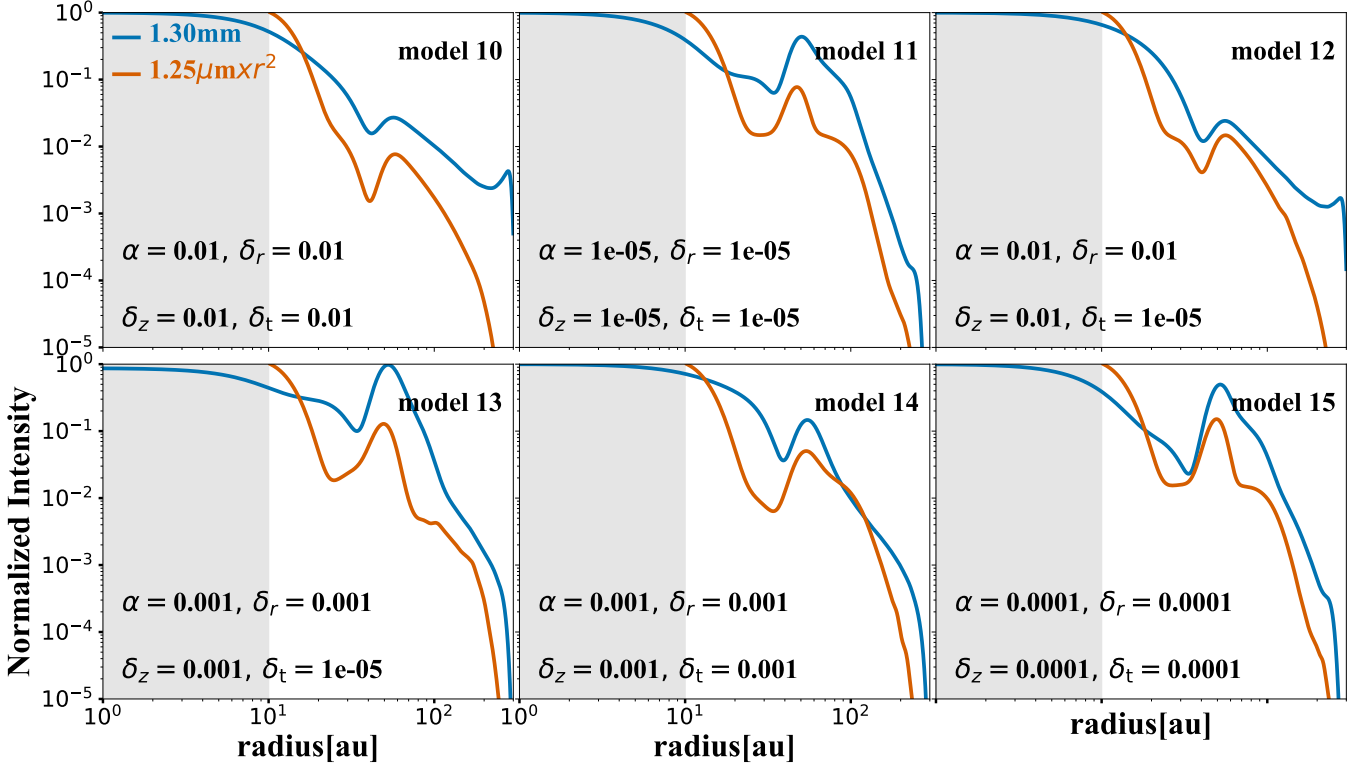


Fig. 8. As Fig. 7 but when a pressure bump is formed in the outer part of the disk.

in the intensity profile at both wavelengths, which contrast is equal or higher in scattered light at  $1.25\ \mu\text{m}$  than in the continuum emission at  $1.3\ \text{mm}$ . This is the opposite result that the long-lived and strong trap, from e.g. giant planet-disk interaction, where the millimeter gaps have higher contrast (e.g., de Juan Ovelar et al. 2013; Dong et al. 2015). In fact, this characteristic of the gaps having higher contrast in scattered light than at the millimeter resembles the results from dust evolution models including the influence of different disk ice-lines (Pinilla et al. 2017a), where trapping does not occur but instead there is a traffic jam effect that originates from the dust particles changing their size at the location of the icelines and hence reducing or increasing their radial drift. The gap in the absence of effective trapping appears due to the local decrease of the maximum grain size at the gap location. In the case that turbulence sets the maximum grain size (model 10 and 14), the contrast of the scattered light gap (measured as the ratio of the emission of the maximum at the outer edge of the gap and the minimum of the intensity at the gap location), is higher than at millimeter, with a contrast of a factor of 10 in scattered light vs. a contrast of a factor of 4-5 at millimeter emission. In the case where there is not trapping and the maximum grain size is set by settling (model 12), the contrast of the gap (a factor of 2) and the width are the same at the two wavelengths.

In the case of effective trapping (models 11, 13, and 15), all the gaps have higher contrast at  $1.3\ \text{mm}$  than at  $1.25\ \mu\text{m}$  as expected from previous models (e.g., de Juan Ovelar et al. 2013). In model 11, the difference in the contrast between the two wavelengths is the lowest, which may have two reasons. First, due to the large grains formed at pressure maximum, whose opacities are low and do not significantly contribute to the  $1.3\ \text{mm}$  emission. Second, since

the gap and the bump are introduced as variations in  $\alpha$ -viscosity and they evolve with viscous time scale, model 11 (with  $\alpha = 10^{-5}$ ) is the one where the gap takes longer to open and reach the final stage, so at  $1\ \text{Myr}$  of evolution, the bump does not have the same amplitude than the other cases.

The contrast of the gap is higher in model 15 ( $\alpha, \delta_{r,z,t} = 10^{-4}$ ) than model 13 ( $\alpha, \delta_{r,z} = 10^{-3}$ , and  $\delta_t = 10^{-5}$ ), because the radial diffusion is lower. Lower dust radial diffusion helps to keep more grains of different size inside the pressure bump, which contributes to increase the contrast in both wavelengths.

In all cases, the gap in scattered light seems to be as narrow or wider than at millimeter emission, which is the opposite from models of trapping with a strong and long-lived pressure bump as the ones expected from giant planets. The nature of this pressure bump forming with viscous timescales and having lower amplitudes leads to this difference. Therefore, the final gap seen in the scattered light in the simulations with a pressure bump may result from a combination of a gap formed purely by dust evolution processes together with effect of the bump in the distribution of the small dust particles. This characteristic of a wider gap in scattered light vs. millimeter emission has been observed in a couple of disks such as TW Hya and HD 163296 (see Fig. 6 in Pinilla et al. 2017a). However, a deeper investigation that studies the influence of the lifetime of the pressure bumps on different disk properties is required to test this conclusion.

## 5. Summary and Conclusions

In this work, we investigate what conditions are required in dust evolution models to grow and trap pebbles in pro-

toplanetary disks when the fragmentation speed is  $1 \text{ m s}^{-1}$  in the entire disk. In particular, we disentangle the parameters controlling the effects of turbulent velocities, vertical stirring, radial diffusion, and gas viscous evolution, always assuming that particles cannot diffuse faster (radially or vertically) than the gas. For some of our simulations, we include a smooth gap in the disk by variations of the  $\alpha$  viscosity parameter, which leads to a pressure bump in the outer disk ( $\sim 52 \text{ au}$ ). The simplified model by [Birnstiel et al. \(2012\)](#) does not include the effects of settling dominated relative particle speeds. Furthermore, for the drift limit they do not consider radial drift dominated growth. We extended the potential growth limits, including the effects of relative speeds dominated by settling, radial drift, and two different turbulence regimes. The calculations are shown in Appendix A. We compare our models with observations of protoplanetary disks at both the near-infrared and millimeter regimes. Our main conclusions are:

- With isotropic turbulence pebble formation can happen in disks when the gas and dust diffusion is low, with values of  $10^{-5} - 10^{-4}$ . Otherwise, pebble formation does not happen and it is not possible to have efficient accumulation of particles in a pressure bump.
- When relative velocities due to turbulence or radial drift are low, settling can dominate the total relative velocities and it can set the maximum grain size. In these cases pebble formation is not possible when  $\delta_z > 10^{-3}$ , which also limits the efficiency of trapping when a pressure bump is present.
- In general, the millimeter fluxes are lower when pebbles are not formed. For all the cases, there is no correlation between the processes that set the maximum grain size and the obtained fluxes. All of the fluxes are within the observed values of the disks in different star forming regions around T-Tauri stars. The fluxes do not change significantly when a trap is included.
- Most of the spectral indices in our work are much higher than observed because the amount of pebbles is too low due to effective drift. Even in the case of models with one pressure bump and effective trapping, the spectral indices are higher than observed. To solve the discrepancy multiple bumps assist to decrease  $\alpha_{\text{mm}}$ . How the bumps are formed and the formation time also have an effect in the spectral index. Static multiple pressure bumps produce lower spectral indices than the models where the gaps and bumps are introduced as variations of  $\alpha$ -viscosity.
- Models without pressure bumps span a large range of synthetic values of  $R_{\text{dust},68\%}$ , that are in agreement with the values in different star forming regions. When comparing models with and without a pressure bump, the dust radii increase for models with a bump, and this increase becomes higher when trapping is efficient.
- One of our simulations without a pressure bump (model 1, see Table 1) produces a large disk as a consequence of the high turbulence, high radial diffusion, and high  $\alpha$  that makes the disk to spread and drag particles along. High turbulence limits the formation of pebbles and small grains are continuously produced by fragmentation that are easier to radially diffuse. This result would imply that disks can appear large when observed at millimeter emission without the need of any pressure bump. Deeper observations at high angular resolu-

tion are needed to test this idea and exclude that substructures are the reason for a potential large size of a disk. In the case of a bump and effective trapping, high radial diffusion also helps to widen the concentration of large particles in pressure maxima.

- As found in [Birnstiel et al. \(2015\)](#), even in the absence of any perturbation in the disk or pressure bump, a large gap is formed in the synthetic scattered light images at  $1.25 \mu\text{m}$ . For all our models, the minimum of this gap is located around  $\sim 25 \text{ au}$  with a similar width (extend up to  $\sim 60\text{-}80 \text{ au}$ ) and contrast (a factor of 10).
- In the cases when a pressure bump is included but there is not effective trapping, there is a gap in the intensity profile at short and long wavelengths, which contrast is equal or higher in scattered light than at millimeter emissions. These results are similar to traffic jam models, e.g. to the dust evolution simulations that include the effect of different disk ice-lines. This is the opposite result of effective trapping by a long-lived and strong trap, e.g. from giant planet-disk interaction, where the millimeter gaps have higher contrast.

## Acknowledgements

We are thankful to the referee for the constructive report. P.P. acknowledges support provided by the Alexander von Humboldt Foundation in the framework of the Sofja Kovalevskaja Award endowed by the Federal Ministry of Education and Research. C.L. was in parts funded by the Deutsche Forschungsgemeinschaft (DFG, German Research Foundation) as part of the Schwerpunktprogramm (SPP, Priority Program) SPP 1833 “Building a Habitable Earth”. We are thankful to A. Pohl for her insightful help with the coupling of dust evolution models and RADMC-3D. We thank S. Stammer for providing us access to `dustpy`.

## References

- Andrews, S. M. 2020, arXiv e-prints, arXiv:2001.05007
- Andrews, S. M., Huang, J., Pérez, L. M., et al. 2018b, *ApJ*, 869, L41
- Avenhaus, H., Quanz, S. P., Garufi, A., et al. 2018, *ApJ*, 863, 44
- Bai, X.-N. 2016, *ApJ*, 821, 80
- Birnstiel, T. & Andrews, S. M. 2014, *ApJ*, 780, 153
- Birnstiel, T., Andrews, S. M., Pinilla, P., & Kama, M. 2015, *ApJ*, 813, L14
- Birnstiel, T., Dullemond, C. P., & Brauer, F. 2010b, *A&A*, 513, A79
- Birnstiel, T., Fang, M., & Johansen, A. 2016, *Space Sci. Rev.*, 205, 41
- Birnstiel, T., Klahr, H., & Ercolano, B. 2012, *A&A*, 539, A148
- Birnstiel, T., Ricci, L., Trotta, F., et al. 2010, *A&A*, 516, L14
- Blum, J. & Wurm, G. 2000, *Icarus*, 143, 138
- Blum, J. & Wurm, G. 2008, *ARA&A*, 46, 21
- Brauer, F. 2008, PhD thesis, Ruperto-Carola University Heidelberg
- Brauer, F., Dullemond, C. P., & Henning, T. 2008, *A&A*, 480, 859
- Davis, S. W., Stone, J. M., & Pessah, M. E. 2010, *ApJ*, 713, 52
- de Juan Ovelar, M., Min, M., Dominik, C., et al. 2013, *A&A*, 560, A111
- Dong, R., Zhu, Z., & Whitney, B. 2015, *ApJ*, 809, 93
- Draine, B. T. 2003, *ApJ*, 598, 1026
- Drążkowska, J., Li, S., Birnstiel, T., Stammer, S. M., & Li, H. 2019, *ApJ*, 885, 91
- Dullemond, C. P., Birnstiel, T., Huang, J., et al. 2018, *ApJ*, 869, L46
- Dullemond, C. P. & Dominik, C. 2004, *A&A*, 421, 1075
- Dullemond, C. P., Juhasz, A., Pohl, A., et al. 2012, RADMC-3D: A multi-purpose radiative transfer tool
- Epstein, P. S. 1924, *Phys. Rev.*, 23, 710
- Flaherty, K., Hughes, A. M., Simon, J. B., et al. 2020, *ApJ*, 895, 109
- Flaherty, K. M., Hughes, A. M., Rose, S. C., et al. 2017, *ApJ*, 843, 150
- Flaherty, K. M., Hughes, A. M., Rosenfeld, K. A., et al. 2015, *ApJ*, 813, 99

- Flock, M., Henning, T., & Klahr, H. 2012, *ApJ*, 761, 95
- Flock, M., Ruge, J. P., Dzyurkevich, N., et al. 2015, *A&A*, 574, A68
- Flock, M., Turner, N. J., Nelson, R. P., et al. 2020, *ApJ*, 897, 155
- Fromang, S. & Nelson, R. P. 2006, *A&A*, 457, 343
- Gundlach, B. & Blum, J. 2015, *ApJ*, 798, 34
- Gundlach, B., Schmidt, K. P., Kreuzig, C., et al. 2018, *MNRAS*, 479, 1273
- Hendler, N., Pascucci, I., Pinilla, P., et al. 2020, *ApJ*, 895, 126
- Kataoka, A., Muto, T., Momose, M., et al. 2015, *ApJ*, 809, 78
- Kimura, H., Wada, K., Kobayashi, H., et al. 2020, *MNRAS*, 498, 1801
- Kimura, H., Wada, K., Senshu, H., & Kobayashi, H. 2015, *ApJ*, 812, 67
- Klahr, H. & Bodenheimer, P. 2006, *ApJ*, 639, 432
- Klahr, H. & Hubbard, A. 2014, *ApJ*, 788, 21
- Klahr, H. & Schreiber, A. 2020, *ApJ*, 901, 54
- Kornet, K., Stepinski, T. F., & Różyczka, M. 2001, *A&A*, 378, 180
- Lenz, C. T., Klahr, H., & Birnstiel, T. 2019, *ApJ*, 874, 36
- Liu, H. B. 2019, *ApJ*, 877, L22
- Long, F., Herczeg, G. J., Harsono, D., et al. 2019, *ApJ*, 882, 49
- Lynden-Bell, D. & Pringle, J. E. 1974, *MNRAS*, 168, 603
- Lyra, W. 2014, *ApJ*, 789, 77
- Manara, C. F., Natta, A., Rosotti, G. P., et al. 2020, *A&A*, 639, A58
- Musiolik, G., Teiser, J., Jankowski, T., & Wurm, G. 2016, *ApJ*, 827, 63
- Musiolik, G. & Wurm, G. 2019, *ApJ*, 873, 58
- Nelson, R. P., Gressel, O., & Umurhan, O. M. 2013, *MNRAS*, 435, 2610
- Ormel, C. W. & Cuzzi, J. N. 2007, *A&A*, 466, 413
- Pinilla, P., Benisty, M., Birnstiel, T., et al. 2014, *A&A*, 564, A51
- Pinilla, P., Birnstiel, T., Benisty, M., et al. 2013, *A&A*, 554, A95
- Pinilla, P., Birnstiel, T., Ricci, L., et al. 2012, *A&A*, 538, A114
- Pinilla, P., Pascucci, I., & Marino, S. 2020, *A&A*, 635, A105
- Pinilla, P., Pohl, A., Stammler, S. M., & Birnstiel, T. 2017a, *ApJ*, 845, 68
- Pinilla, P., Quiroga-Nuñez, L. H., Benisty, M., et al. 2017b, *ApJ*, 846, 70
- Pinilla, P., van der Marel, N., Pérez, L. M., et al. 2015, *A&A*, 584, A16
- Pohl, A., Kataoka, A., Pinilla, P., et al. 2016, *A&A*, 593, A12
- Pringle, J. E. 1981, *ARA&A*, 19, 137
- Ricci, L., Testi, L., Natta, A., et al. 2010, *A&A*, 512, A15
- Ricci, L., Testi, L., Natta, A., Scholz, A., & de Gregorio-Monsalvo, I. 2012, *ApJ*, 761, L20
- Safronov, V. S. 1969, *Evolutsiia doplanetnogo oblaka*.
- Shakura, N. I. & Sunyaev, R. A. 1973, *A&A*, 500, 33
- Simon, J. B., Armitage, P. J., & Beckwith, K. 2011, *ApJ*, 743, 17
- Smoluchowski, M. V. 1916, *Zeitschrift fur Physik*, 17, 557
- Stammler, S. M., Drażkowska, J., Birnstiel, T., et al. 2019, *ApJ*, 884, L5
- Steinpilz, T., Teiser, J., & Wurm, G. 2019, *ApJ*, 874, 60
- Stepinski, T. F. & Valageas, P. 1997, *A&A*, 319, 1007
- Stoll, M. H. R. & Kley, W. 2014, *A&A*, 572, A77
- Teague, R., Guilloteau, S., Semenov, D., et al. 2016, *A&A*, 592, A49
- Teague, R., Henning, T., Guilloteau, S., et al. 2018, *ApJ*, 864, 133
- Tripathi, A., Andrews, S. M., Birnstiel, T., & Wilner, D. J. 2017, *ApJ*, 845, 44
- Turner, N. J., Fromang, S., Gammie, C., et al. 2014, in *Protostars and Planets VI*, ed. H. Beuther, R. S. Klessen, C. P. Dullemond, & T. Henning, 411
- Wada, K., Tanaka, H., Suyama, T., Kimura, H., & Yamamoto, T. 2009, *ApJ*, 702, 1490
- Wada, K., Tanaka, H., Suyama, T., Kimura, H., & Yamamoto, T. 2011, *ApJ*, 737, 36
- Warren, S. G. & Brandt, R. E. 2008, *Journal of Geophysical Research: Atmospheres*, 113 [https://agupubs.onlinelibrary.wiley.com/doi/pdf/10.1029/2007JD009744]
- Whipple, F. L. 1972, in *From Plasma to Planet*, ed. A. Elvius, 211
- Windmark, F., Birnstiel, T., Güttler, C., et al. 2012, *A&A*, 540, A73
- Youdin, A. N. & Lithwick, Y. 2007, *Icarus*, 192, 588
- Zhu, Z., Zhang, S., Jiang, Y.-F., et al. 2019, *ApJ*, 877, L18
- Zubko, V. G., Mennella, V., Colangeli, L., & Bussoletti, E. 1996, *MNRAS*, 282, 1321

## Appendix A: Growth Barrier Estimates

In this appendix we provide analytical prescriptions for different growth barriers, which depend on the relative speed among the largest grains. We assume mono-disperse growth for non-vanishing relative velocities for equal-sized particles and duo-disperse growth where relative velocities of particles of the same size is zero. In the latter case, we model growth assuming that the mass dominating species grows via collisions of particles that are  $N$  times smaller. We model the relative speed due to radial drift ( $\Delta v_r$ ), azimuthal drift ( $\Delta v_\varphi$ ), vertical settling ( $\Delta v_z$ ), and turbulent motion ( $\Delta v_{\text{turb II}}$ ), respectively as

$$\Delta v_r \approx \frac{c_s^2}{v_K} \left| \frac{\partial \ln P}{\partial \ln r} \right| (1-N) \text{St}, \quad (\text{A.1})$$

$$\Delta v_\varphi \approx \frac{1}{2} \frac{c_s^2}{v_K} \left| \frac{\partial \ln P}{\partial \ln r} \right| \left| \frac{1}{\text{St}^2 + 1} - \frac{1}{N^2 \text{St}^2 + 1} \right|, \quad (\text{A.2})$$

$$\Delta v_z \approx h_d \Omega (1-N) \text{St} = c_s (1-N) \frac{\text{St}}{\sqrt{1 + \text{St}/\delta_z}}, \quad (\text{A.3})$$

$$\Delta v_{\text{turb II}} \approx \sqrt{3\delta_t \text{St} c_s}. \quad (\text{A.4})$$

These are approximations for the different contributions to the relative speed if  $\text{St} < 1$  and if the azimuthal pressure gradient is zero. For the second turbulent regime, particles are required to have Stokes numbers larger than  $1/\sqrt{\text{Re}}$ , where the Reynolds number is given by

$$\begin{aligned} \text{Re} &= \frac{\nu_{\text{turb}}}{\nu_{\text{mol}}} \approx \frac{\sqrt{\pi} \delta_t c_s}{\Omega \sqrt{2} \lambda} \\ &= \frac{\sqrt{\pi} \delta_t n \sigma_{\text{H}_2} c_s}{\Omega} \stackrel{z=0}{\approx} \frac{\delta_t \Sigma_g \sigma_{\text{H}_2}}{\sqrt{2} m_g}. \end{aligned} \quad (\text{A.5})$$

Here, we adopted the cross section of molecular hydrogen  $\sigma_{\text{H}_2} \approx 2 \times 10^{-5} \text{ cm}^2$

and assumed that the mean molecular weight  $m_g$  is about 2.3 proton masses, which is roughly

$$m_{\text{proton}} \approx 1.67 \times 10^{-24} \text{ g}. \quad (\text{A.7})$$

The mean free path of gas molecules following the Maxwell-Boltzmann distribution is given by

$$\lambda = \frac{1}{\sqrt{2}} \frac{1}{n \sigma_{\text{H}_2}} \quad (\text{A.8})$$

with number density of gas molecules  $n$ . We assume that the collisional behavior can be modeled by collision partners with a factor of  $N \approx 0.5$  difference in Stokes number (however, see comments at the end of this Appendix). The factor that depends on the Stokes number in the expression of the the relative azimuthal drift  $\Delta v_\varphi$  needs simplifications to find simple analytical expressions for the growth barriers for which the relative speed among the largest grains is dominated by this effect. This expression can be simplified by neglecting higher order terms as follows:

$$\left| \frac{1}{\text{St}^2 + 1} - \frac{1}{N^2 \text{St}^2 + 1} \right| = \frac{(1-N^2) \text{St}^2}{N^2 \text{St}^4 + (1+N^2) \text{St}^2 + 1} \quad (\text{A.9})$$

The fragmentation limit can be estimated by setting the dominating relative speed equal to the critical fragmentation speed  $v_f$  (Birnstiel et al. 2010b, 2012). For the case of

relative speeds dominated by radial drift this yields (Birnstiel et al. 2012)

$$\text{St}_{\text{frag},r} = \frac{v_f v_K}{c_s^2} \left| \frac{\partial \ln P}{\partial \ln r} \right|^{-1} \frac{1}{1-N}. \quad (\text{A.10})$$

By neglecting the  $\mathcal{O}(\text{St}^2)$  term in the denominator on the right side of Eq. (A.9), the fragmentation limit in the case of relative speeds dominated by azimuthal drift can be estimated to be

$$\text{St}_{\text{frag},\varphi} = \sqrt{2} \frac{v_f v_K}{c_s^2} \left| \frac{\partial \ln P}{\partial \ln r} \right|^{-1} \frac{1}{1-N^2}. \quad (\text{A.11})$$

However, the relative velocities due to azimuthal drift of the largest grains with similar-sized grains for  $\text{St} < 1$  are expected to be smaller than those caused by relative radial drift:

$$\Delta v_\varphi \approx \frac{1-N^2}{2(1-N)} \text{St} \Delta v_r < \Delta v_r. \quad (\text{A.12})$$

For settling dominated relative speeds a quadratic equation of the following form is achieved:

$$\text{St}^2 - \text{St} \frac{A}{\delta_z} - A = 0, \quad (\text{A.13})$$

where

$$A := \frac{v_f^2}{c_s^2 (1-N)^2}. \quad (\text{A.14})$$

The physical solution is found to be

$$\text{St}_{\text{frag},z} = \frac{A}{2\delta_z} + \sqrt{\frac{A^2}{4\delta_z^2} + A}. \quad (\text{A.15})$$

The fragmentation limit in the turbulence dominated regime is given by (Birnstiel et al. 2010, 2012)

$$\text{St}_{\text{frag,turb}} = \frac{1}{3} \frac{v_f^2}{\delta_t c_s^2}. \quad (\text{A.16})$$

Since higher relative velocities lead to the critical fragmentation speed at smaller sizes, the overall fragmentation limit can be estimated via

$$\text{St}_{\text{frag}} = \min \{ \text{St}_{\text{frag,turb}}; \text{St}_{\text{frag},r}; \text{St}_{\text{frag},z} \}. \quad (\text{A.17})$$

The drift limit can be obtained by setting the growth timescale

$$\tau_{\text{grow}} = 2\sqrt{2\pi} \frac{\rho_s h_g}{\Sigma_d} \frac{a}{\sqrt{1 + \text{St}/\delta_z} \Delta v} \quad (\text{A.18})$$

and drift timescale

$$\tau_{\text{drift}} = \frac{r}{|v_{\text{drift}}|} = \frac{\text{St}^{\mathcal{Z}} + 1}{\text{St}} \frac{r v_K}{c_s^2} \left| \frac{\partial \ln P}{\partial \ln r} \right|^{-1} \quad (\text{A.19})$$

equal to each other (Klahr & Bodenheimer 2006; Birnstiel et al. 2012). In the derivation of this growth timescale, we assumed a growth rate (particle radius per time) that is half as high as in canonical derivations from Stepinski & Valageas (1997) and Kornet et al. (2001). When using the

Smoluchowski equation, a factor of 0.5 naturally shows up in the growth rate (e.g., Brauer 2008). This growth timescale is an estimate for mono-disperse growth only. However, it is still good enough to estimate the growth barriers which can be fine-tuned with fudge factors or via the  $N$  parameter.

With help of the Stokes number in the midplane in the Epstein drag regime Eq. (1), the growth timescale can be written in a form independent of particle radius  $a$ :

$$\tau_{\text{grow}} = 4\sqrt{\frac{2}{\pi}} \frac{h_g}{\Delta v} \frac{1}{Z} \frac{\text{St}}{\sqrt{1 + \text{St}/\delta_z}}, \quad (\text{A.20})$$

where  $Z := \Sigma_d/\Sigma_g$  is the column density ratio of all particles to gas. By neglecting second order terms in Stokes number, the relative speed due to radial drift can be written as

$$\Delta v_r \approx (1 - N)|v_{\text{drift}}|. \quad (\text{A.21})$$

Setting the growth and drift timescales equal leads to the quadratic equation

$$\text{St}^2 - \frac{B}{\delta_z} \text{St} - B = 0, \quad (\text{A.22})$$

where

$$B := \left( \frac{\pi(1 - N)}{4\sqrt{2\pi}} \frac{v_K}{c_s} Z \right)^2. \quad (\text{A.23})$$

The physical solution yields the drift limit in the radial drift dominated growth regime

$$\text{St}_{\text{drift},r} = \frac{B}{2\delta_z} + \sqrt{\frac{B^2}{4\delta_z^2} + B}. \quad (\text{A.24})$$

By assuming settling dominated relative velocities, we obtain

$$\text{St}_{\text{drift},z} = \frac{\sqrt{\pi}}{4\sqrt{2}} (1 - N) Z \left( \frac{v_K}{c_s} \right)^2 \left| \frac{\partial \ln P}{\partial \ln r} \right|^{-1}. \quad (\text{A.25})$$

The case of dominating relative azimuthal drift is not interesting due to Eq. (A.12). For turbulent motion as dominating source of relative velocities, equating the growth and drift timescale yields after squaring both sides

$$\frac{\text{St}^2}{\delta_t/\text{St} + \delta_t/\delta_z} = \sqrt{\frac{3\pi}{32}} Z \left( \frac{v_K}{c_s} \right)^2 \left| \frac{\partial \ln P}{\partial \ln r} \right|^{-1}, \quad (\text{A.26})$$

which gives (for  $\text{St} \gg \delta_z$ )

$$\text{St}_{\text{drift,turb II}} = \sqrt{\frac{3\pi}{32}} \sqrt{\frac{\delta_t}{\delta_z}} Z \left( \frac{v_K}{c_s} \right)^2 \left| \frac{\partial \ln P}{\partial \ln r} \right|^{-1}. \quad (\text{A.27})$$

According to Ormel & Cuzzi (2007) particles with  $\text{St} < \text{Re}^{-1/2}$  are in the first turbulent regime—this regime can be reached in the very outer parts of circumstellar disks—with relative speed

$$\begin{aligned} \Delta v_{\text{turb I}} &\approx \sqrt{\delta_t} c_s \sqrt{\frac{1 - N}{1 + N}} \\ &\times \underbrace{\sqrt{\frac{\text{St}^2}{\text{St} + \text{Re}^{-1/2}} - \frac{N^2 \text{St}^2}{N \text{St} + \text{Re}^{-1/2}}}}_{\approx \sqrt{(1 - N^2) \text{Re}^{1/4} \text{St}}} \\ &\approx \sqrt{\delta_t} c_s (1 - N) \text{Re}^{1/4} \text{St}. \end{aligned} \quad (\text{A.28})$$

**Table A.1.** Values of parameters of relative Stokes number  $N$  between favorable collision partners used to model the maximum size in different regimes of relative speed.

$\Delta v$ regime	$N$ in drift limit	$N$ in frag. limit
turb I	0.1, Eq. (A.30)	–
turb II	1.0, Eq. (A.27)	1.0, Eq. (A.16)
rad. drift	0.8, Eq. (A.24)	0.3, Eq. (A.10)
settling	0.8, Eq. (A.25)	0.3, Eq. (A.15)

Following the same steps as above to obtain the drift limit, the same quadratic equation as Eq. (A.22) with the solution Eq. (A.24) is obtained but for  $B \rightarrow C$  with

$$C := \frac{\pi}{32} \left( \frac{v_K}{c_s} \right)^4 Z^2 \left| \frac{\partial \ln P}{\partial \ln r} \right|^{-2} \delta_t (1 - N)^2 \sqrt{\text{Re}}. \quad (\text{A.29})$$

The solution is given by

$$\text{St}_{\text{drift,turb I}} = \frac{C}{2\delta_z} + \sqrt{\frac{C^2}{4\delta_z^2} + C}. \quad (\text{A.30})$$

Due to the different scaling of the relative velocities, this drift limit  $\text{St}_{\text{drift,turb I}}$  fits the simulation results better for  $N = 0.1$ . The overall drift limit in the turbulence dominated case is estimated as

$$\text{St}_{\text{drift,turb}} = \begin{cases} \text{St}_{\text{drift,turb II}} & , \text{St}_{\text{drift,turb I}} \geq \text{Re}^{-1/2} \\ \text{St}_{\text{drift,turb I}} & , \text{St}_{\text{drift,turb I}} < \text{Re}^{-1/2} \end{cases}. \quad (\text{A.31})$$

Since faster growth caused by higher relative velocities leads to shorter growth timescales, the overall drift limit is given by

$$\text{St}_{\text{drift}} = \max \{ \text{St}_{\text{drift,turb}}; \text{St}_{\text{drift},r}; \text{St}_{\text{drift},z} \}. \quad (\text{A.32})$$

Both the fragmentation limit Eq. (A.17) and the drift limit Eq. (A.32) can be converted to particle radii by using the  $\text{St}-a$  relation in the Epstein regime Eq. (1).

The  $N$  parameter can potentially be different for the fragmentation limit or drift limit since this depends on the size distribution, which is different in those limits. While the size distribution in drift limited regions is very top-heavy, fragmentation limited regions show shallower size distributions. In the most cases,  $N = 0.3$  for fragmentation limits and  $N = 0.8$  for drift limits mimic the evolution of the maximum grain size quite well. We summarize the values used for  $N$  in different cases in Tab. A.1. Especially the fragmentation limits do a great job. The drift limit at late times and in the most outer regions of the disk can significantly deviate from the data of numerical simulations. This could be an effect of violated conditions for the analytical estimates (e.g. relative speeds are not dominated by one effect, or the size distribution does not allow an almost mono-disperse or duo-disperse approach).